
This is a partially peer reviewed preprint submitted to EarthArXiv.
This manuscript has completed one round of peer review with
Remote Sensing of Environment and includes corresponding revisions.
Subsequent peer-reviewed versions may have different content.
The authors welcome feedback.

Robust Probabilities of Detection and Quantification Uncertainty for Aerial Methane Detection: Examples for Three Airborne Technologies

Bradley M. Conrad, David R. Tyner, Matthew R. Johnson*

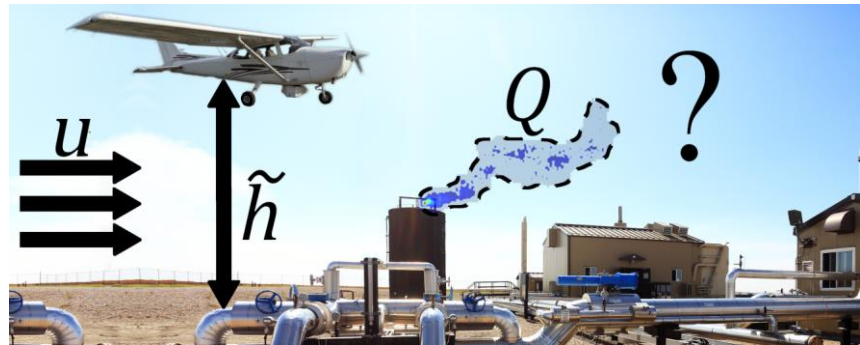
*Energy & Emissions Research Laboratory,
Department of Mechanical and Aerospace Engineering,
Carleton University, Ottawa, ON, Canada, K1S 5B6*

KEYWORDS: Methane; remote sensing; aerial detection sensitivity; quantification uncertainty; monitoring, reporting, and verification; MRV; oil and gas; AMEL; Alt-FEMP; measurement-based inventories; fugitive emissions

*CORRESPONDING AUTHOR: Matthew.Johnson@carleton.ca; +1-613-520-2600 ext.4039

Abstract

Thorough characterization of probabilities of detection (POD) and quantification uncertainties is fundamentally important to understand the place of aerial measurement technologies in alternative means of emission



limitation (AMEL) or alternate fugitive emissions management programs (Alt-FEMP); monitoring, reporting, and verification (MRV) efforts; and surveys designed to support measurement-based emissions inventories and mitigation tracking. This paper presents a robust framework for deriving continuous probability of detection functions and quantification uncertainty models for example aerial measurement techniques based on controlled release data. Using extensive fully- and semi-blinded controlled release experiments to test Bridger Photonics Inc.'s Gas Mapping LiDAR (GML)TM, as well as available semi- and non-blinded controlled release data for Kairos LeakSurveyorTM and NASA/JPL AVIRIS-NG technologies, robust POD functions are derived that enable calculation of detection probability for any given source rate, wind speed, and flight altitude. Uncertainty models are separately developed that independently address measurement bias, bias variability, and measurement precision, allowing for a distribution of the true source rate to be directly calculated from the source rate estimated by the technology. Derived results demonstrate the potential of all three technologies in methane detection and mitigation, and the developed methodology can be readily applied to characterize other techniques or update POD and uncertainty models following future controlled release experiments. Finally, the analyzed results also demonstrate the importance of

34 using controlled release data from a range of sites and times to avoid underestimating measurement
35 uncertainties.

36 **Highlights**

- 37 • Generalized method presented to derive aerial methane detection sensitivity
- 38 • Generalized error model also developed to derive quantification uncertainty
- 39 • Continuous probability of detection functions derived for three aerial technologies
- 40 • Results give detection probability for any source, wind, and flight altitude
- 41 • Enables use of aerial data in MRV, AMEL/Alt-FEMP, and measurement-based inventories

42 **1 Introduction**

43 Methane is a potent yet short-lived greenhouse gas and rapid reductions in methane emissions from energy,
44 waste, and agriculture sectors are an essential part of the pathway to limiting global temperature rise (Arias
45 et al., 2021; CCAC, 2021; IPCC, 2018). However, successful mitigation of emissions is contingent on the
46 ability to reliably detect potential emissions from both known and unknown sources. Moreover,
47 development of trustworthy emission inventories and tracking progress toward mitigation targets requires
48 accurate measurements within defined uncertainties. This challenge is central to emerging monitoring,
49 reporting and verification (MRV) efforts (European Commission, 2021) and the associated verification role
50 of the United Nations International Methane Emissions Observatory (IMEO).

51 In recent years, a range of potential detection and/or measurement technologies have been explored
52 with promise to significantly reduce time and labour costs to find and measure sources of methane,
53 especially for applications in the oil and gas sector (Bell et al., 2020; Fox et al., 2019; Kemp and Ravikumar,
54 2021; Rashid et al., 2020; Ravikumar et al., 2019; Schwietzke et al., 2019). Of particular interest are
55 airplane-mounted technologies, which are increasingly used in large-scale field campaigns with success
56 (Chen et al., 2022; Cusworth et al., 2021; Tyner and Johnson, 2021) and gaining acceptance in alternate
57 fugitive emissions management programs (Alt-FEMP) replacing or supplementing optical gas imaging
58 (OGI) surveys using hand-held infrared cameras (AER, 2021; Bridger Photonics, 2022; InvestableUniverse,
59 2021; Kairos Aerospace, 2022a). With sensitivities >100-1000 times better than current satellite systems,
60 airplane-mounted sensors have emerged as a key tool for mitigating methane, well-suited to the challenging
61 “verification” component of MRV and capable of being used to create measurement-based inventories.
62 However, successful application of these technologies and interpretation of collected data requires a
63 thorough understanding of the probability of detecting unknown sources under different conditions and
64 uncertainty in quantifying emissions from detected sources. To date, only limited controlled release studies

65 have appeared in the literature (Bell et al., 2020; Johnson et al., 2021; Ravikumar et al., 2019; Sherwin et
66 al., 2021; Thorpe et al., 2016) and robust methodologies to meet these requirements have not been
67 developed.

68 This paper has four main objectives. First, a novel generalized approach to deriving continuous
69 probability of detection (POD) functions is presented that significantly improves upon existing formulations
70 in the literature that are often non-physical. Generalized POD functions are essential for understanding
71 what is or is not captured in field measurements and modelling applicability and mitigation potential of
72 technologies in programs like FEAST (Fugitive Emissions Abatement Simulation Toolkit; Kemp et al.,
73 2016). Second, a statistical error model is presented to derive quantification uncertainties in aerial-
74 estimated source rates. Together with robust POD data, quantification uncertainties are essential for
75 defensibly applying airborne measurements for MRV and ultimately for using aerial data in measurement-
76 based inventories. Third, using extensive controlled release experiments completed to evaluate Bridger
77 photonics' gas mapping LiDAR (GML)TM system (Bridger Photonics, 2021) as an initial case study, a
78 continuous POD function and quantification uncertainty model are derived. Finally, using available
79 published controlled release data, the methods are extended to also estimate robust POD and quantification
80 uncertainty of Kairos LeakSurveyorTM (Kairos Aerospace, 2022b) and POD of NASA's Jet Propulsion
81 Laboratory's Next-Generation Airborne Visible/Infrared Imaging Spectrometer (AVIRIS-NG) platform
82 (Thorpe et al., 2016).

83 **2 Methodology**

84 ***2.1 Methane Detection Technologies***

85 ***2.1.1 Bridger Photonics Gas Mapping LiDARTM***

86 Bridger Photonics Gas Mapping LiDAR (GML) uses an airplane-mounted scanning laser, camera, and
87 Global Navigation Satellite System – Inertial Navigation System to detect methane sources and produce
88 quantitative geo-located imagery of associated plumes (Bridger Photonics, 2021; Hunter and Thorpe, 2017;
89 Johnson et al., 2021; Kreitinger and Thorpe, 2018). Originally developed through the Advanced Research
90 Project Agency – Energy (ARPA-E) MONITOR program (ARPA-E, 2018), the technology uses
91 wavelength modulation spectroscopy at 1651 nm to measure path-integrated methane concentrations
92 between the aircraft and the ground, which acts as a topographic backscatterer. Forward and backward
93 looking measurements as the plane flies give information on the detected plume height, typically within
94 2 m accuracy (Johnson et al., 2021). At typical target altitudes between 168 and 230 m above ground level
95 (AGL), the sensor's 31° field-of-view results in an approximately 94–130 m wide measurement swath on
96 the ground and resolves plumes with ~1–2 m spatial resolution. Source emission rates are estimated by a

97 proprietary method that combines information about the spatial concentration of methane in the detected
98 plume, the height of the plume above ground level, the horizontal wind speed at the time of detection
99 (Bridger Photonics typically uses interpolated hourly meteorological station data from the public High-
100 Resolution Rapid Refresh (HRRR) database (NOAA, 2020) or Meteoblue ([meteoblue.com](https://www.meteoblue.com)) depending on
101 coverage in the region of interest), and the assumed vertical profile of wind speed. Preliminary analysis of
102 blinded controlled releases by Johnson et al., (2021) suggests that 1σ quantification uncertainties of ± 31 –
103 68% can be expected from a single pass of sources near the sensitivity limit. However, uncertainties at
104 higher release rates and over a broader range of conditions are not well-described in the literature and a
105 robust understanding of these uncertainties is an important goal of this paper.

106 2.1.2 Kairos Aerospace LeakSurveyor™

107 Kairos Aerospace's LeakSurveyor is an airplane-mounted methane imaging system that combines an
108 infrared imaging spectrometer, global positioning system (GPS) and inertial monitoring unit, and optical
109 camera to detect methane plumes (Berman et al., 2021; Branson et al., 2021; Schwietzke et al., 2019). Path-
110 integrated methane concentrations are measured via absorption of reflected sunlight from the ground in
111 spectral regions where there is no interference from other common hydrocarbons (Berman et al., 2021).
112 For the targeted flight altitude of 900 m AGL, each measurement swath is approximately 800 m wide with
113 a spatial resolution of ~ 3 m (Sherwin et al., 2021). As summarized in Berman et al. (2021) and Sherwin et
114 al. (2021), quantification is via a proprietary algorithm that calculates pixel-level methane column density
115 between the airplane and the ground, sums these estimates within a core-plume region with distinguishable
116 methane enhancements from background, divides by the length of this core plume region, and multiplies
117 by an estimated wind speed. Compared to Bridger Photonics' *active* GML sensor, the *passive*
118 LeakSurveyor from Kairos Aerospace trades potential advantages of larger measurement swath permitting
119 greater facility coverage per airplane pass with the disadvantages of lower spatial resolution and higher
120 minimum detection limits as well as potentially greater sensitivity to environmental lighting conditions.

121 Because in-situ wind speed is not generally available for aircraft-detected sources and database wind
122 speed can be highly uncertain, Kairos Aerospace typically provides source rate estimates on a wind-
123 normalized basis – i.e., in units of emission rate per wind speed (Branson et al., 2021). Kairos' in-house
124 (Berman et al., 2021) and third-party (Sherwin et al., 2021) assessments of the LeakSurveyor technology
125 have estimated detection sensitivities in these units of approximately 8.2 (at a 50% POD) and
126 5-15 (kg/h)/(m/s) ("partial detection range"), respectively. Quantification bias was also assessed by Kairos
127 Aerospace on a wind-normalized source rate-basis and found to be approximately -2% (Branson et al.,
128 2021); precision errors were not analyzed. In their controlled release study, Sherwin et al., (2021)
129 independently evaluated quantification error in emission rate (non-normalized units of kg/h) by multiplying

130 LeakSurveyor-reported wind-normalized source rate data by wind speed estimated from four different
131 sources. The parity slope of estimated-to-controlled source rates ranged from 0.88 to 1.45×, representing
132 a bias on the order of −12 to +45% depending on the source of wind speed data. Precision errors were
133 estimated using the residuals of linear fits to controlled release data and were on the order of 30-42% (1σ).

134 *2.1.3 NASA JPL's Next-Generation Airborne Visible/Infrared Imaging Spectrometer*

135 The next-generation airborne visible/infrared imaging spectrometer (AVIRIS-NG; Hamlin et al., 2011) is
136 an improvement on the original AVIRIS instrument (Green et al., 1998) developed by the U.S. National
137 Aeronautics and Space Administration's (NASA) Jet Propulsion Laboratory (JPL). The AVIRIS-NG
138 instrument is a push-broom imaging spectrometer with approximately 5 nm spectral resolution over the
139 visible and near-infrared spectra (380 to 2510 nm). Methane point source detection studies have flown the
140 AVIRIS-NG instrument at different altitudes: 430 to 3800 m AGL (Thorpe et al., 2016) and, more recently,
141 3000 to 8000 m AGL (Thorpe et al., 2021). For the approximately 34° field-of-view, swath widths and
142 spatial resolutions are on the order of 1800 m and 3 m at a typical/common flight altitude of 3000 m AGL
143 (Duren et al., 2019; Thorpe et al., 2021) and approximately 3300 m and 8 m at a flight altitude of
144 8000 m AGL. Methane columns are retrievable using differential optical absorption spectroscopy (e.g.,
145 Cusworth et al., 2019; Thorpe et al., 2017) or matched filter methods (e.g., Foote et al., 2020; Thompson et
146 al., 2015) permitting downstream processing to identify methane plumes.

147 Although the development of AVIRIS(-NG) was not specifically motivated by methane detection,
148 AVIRIS-NG has been successfully used to detect, map, and monitor large-scale methane emitters.
149 Methane-relevant studies have targeted measurements at an array of assorted facility types (Duren et al.,
150 2019; Guha et al., 2020) with some focusing on oil and gas facilities (Cusworth et al., 2021; Frankenberg
151 et al., 2016; Thorpe et al., 2020) solid waste facilities (Cusworth et al., 2020; Krautwurst et al., 2017), and
152 arctic permafrost (Elder et al., 2020). In 2013, Thorpe et al. (2016) mounted the AVIRIS-NG instrument
153 on a Twin Otter aircraft during controlled release experiments to evaluate methane retrieval algorithms and
154 assess detection sensitivity as a function of wind speed and aircraft altitude. At the time of writing, the
155 accuracy of methane source rate estimation using AVIRIS-NG has not been evaluated in detail, although a
156 recent study focusing on the evaluation of an airborne Doppler wind LiDAR instrument (Thorpe et al.,
157 2021) includes source quantification data for a pair of controlled release tests.

158 **2.2 Controlled Releases – Bridger GML**

159 For this study, controlled methane releases were completed as part of two separate field campaigns during
160 September 5-8, 2020 and August 19-22, 2021 at oil production sites near Lloydminster, Saskatchewan to
161 assess Bridger Photonics' GML technology. These releases were completed as part of broader

162 measurement surveys across western Canada and included both semi-blinded and fully blinded experiments
163 to assess quantification accuracy as well as detection sensitivity under varying conditions. First, working
164 collaboratively with Bridger Photonics and the contracted airplane operator, high-flowrate controlled
165 releases were completed to derive GML quantification uncertainties when measuring methane sources
166 emitting between 1 and 66 kg/h, consistent with 96% of sources found in a recent survey of oil and gas
167 infrastructure in BC, Canada (Tyner and Johnson, 2021). These *semi-blinded* releases, where Bridger was
168 told that controlled releases were being performed but not informed of the exact release locations within
169 the facilities nor the flow rates, were made from a set of four inactive oil and gas facilities conveniently
170 arranged in a line approximately 375 m apart (refer to supplemental information (SI) for additional detail).
171 Over four days during each campaign, the plane flew laps over the test facilities while flow rates at each
172 site were independently varied between each lap at predetermined random flow rates (including zero
173 releases) that were not shared with Bridger Photonics nor the aircraft operator.

174 Second, following the same approach used in Johnson et al. (2021), additional low-flowrate controlled
175 releases (0.4–5.2 kg/h) plus zero-releases were performed from active sites included in parallel contracted
176 surveys of oil and gas infrastructure in the region. In collaboration with industry operators, methane was
177 released from within facility premises at random rates near the expected sensitivity limit of the GML
178 technology to test its ability to correctly detect unknown sources at unknown locations. These tests,
179 performed considering impacts from interaction of the temporally varying wind with adjacent infrastructure
180 and in the potential presence of additional sources from the active facilities, were fully blinded in that they
181 were conducted without informing Bridger Photonics nor the aircraft operator that the experiments were
182 taking place. Bridger provided final source detection and quantification data (obtained using their internal
183 analysis of Meteoblue wind data) without having access to data from the semi-blinded releases and without
184 having been informed of the fully blinded release experiments.

185 At each release location time-resolved wind speed at 3 m above ground level was measured at 1 Hz
186 using an ultrasonic wind sensor (Anemoment, TriSonica mini) with a rated accuracy of ± 0.2 m/s over the
187 relevant range of 0–10 m/s. Methane from compressed cylinders (PraxAir, >99% purity) was released
188 through Bronkhorst thermal mass flow controllers (various models, rated accuracy of $\pm 0.1\%$ of full scale
189 or $\pm 0.5\%$ of reading). For the larger flow rates, a custom-built heated regulator and liquid-gas heat
190 exchanger system were used to overcome Joule-Thomson cooling of the gas and ensure temperatures were
191 near ambient as it entered the flow controllers. The methane then flowed through at least ~ 20 m of tubing
192 to a release point from a vertically oriented, 1 m length pipe (i.e., typical working height for oil and gas
193 infrastructure) temporarily secured to the ground. GPS-synchronized data loggers were used to record
194 methane release rate and wind speed data that could subsequently be matched with time-stamped data

195 provided by Bridger. This was especially important in confirming missed detections during the fully
 196 blinded releases from within sites included in the parallel surveys of oil and gas infrastructure. Although
 197 exit temperature of each methane release was not measured, calculations confirm that the length of tubing
 198 was such that it would have been ambient in all cases consistent also with the field experiments of Sherwin
 199 et al. (2021). Table 1 summarizes the collected controlled release data.

200 **Table 1: Summary of Controlled Release Experiments to test Bridger Photonics' GML completed**
 201 **as part of the present study.**

Release Set	Period	Count
High-flowrate (1–66 kg/h), semi-blinded releases from a fixed set of inactive facilities ^a	Sept. 5-8, 2020	138 (122 non-zero)
	Aug. 19-22, 2021	175 (162 non-zero)
Low-flowrate (0.4–5.2 kg/h), fully blinded releases from within active sites included in parallel oil & gas sector surveys ^b	Sept. 5-7, 2020	67 (38 Misses)
	Aug. 19-21, 2021	115 (24 Misses)
Total	495 total releases	

^a All non-zero semi-blinded releases were detected.

^b Representative scene noise was provided with the standard data product for small-volume releases in 2020 and 2021

202

203 **2.3 Available Controlled Release Data for Kairos' LeakSurveyor**

204 Using the new methodology presented below, a robust POD function and uncertainty model were also
 205 developed for Kairos' LeakSurveyor using published controlled release data from Sherwin et al. (2021)
 206 augmented with internal controlled release data obtained from Kairos similar to Chen et al. (2022). Sherwin
 207 et al. (2021) completed 234 semi-blinded controlled release tests of Kairos' LeakSurveyor from a single
 208 facility located in San Joaquin County, California over four days spanning October 8-15, 2019. These
 209 included 210 non-zero controlled releases between 18 to 1,025 kg/h. Three data points were discarded
 210 following Sherwin et al.'s (2021) initial quality control and the remaining 207 releases were used to assess
 211 detection sensitivity in the present work – 40 of these 207 releases were purposely performed at low
 212 flowrates near the lower limit of the flowmeter (<50 kg/h). Of the original 210 releases, 148 were
 213 considered for the present assessment of quantification error, corresponding to the subset of release data
 214 with a successful detection, a controlled rate > 50 kg/h, and no quality control concerns. Wind speeds were
 215 measured in situ at 8 ft (~2.43 m) above ground level using two instruments: a cup-based wind meter and
 216 a two-dimensional ultrasonic anemometer (on the latter three days only). Sherwin et al. (2021)'s analysis
 217 also evaluated quantification error for the practical scenario where in-situ wind speed data are not available,
 218 testing accuracy when using minute-resolved data from the commercial Dark Sky database (Apple Inc.,

219 2022) and hourly data from the HRRR database (NOAA, 2020). The LeakSurveyor sensor was used to
220 detect and, where possible, quantify the controlled releases and was flown at a nominal altitude of
221 900 m AGL throughout the study. For the present analysis of POD, in-situ wind speed from the ultrasonic
222 anemometer is favoured when available due to its improved accuracy over the cup-based meter; for the
223 measurement day where only data from the cup-meter were available, these data are corrected based on a
224 linear fit with available ultrasonic data. Sherwin et al. (2021) chose the one-minute gust as the
225 representative measured wind speed (corresponding to the maximum speed during the minute prior to the
226 aircraft overpass) in the main text of their analysis, which matches the wind speed preferred in Kairos'
227 quantification as further discussed below. By contrast, the present analysis uses the one-minute *averaged*
228 wind speed prior to the aircraft overpass as it is likely to be more indicative of convective dispersion of the
229 plume prior to detection and is the relevant windspeed to consider when planning a survey or modelling
230 expected performance in simulators like FEAST. To standardize wind speeds against the present controlled
231 releases, all available wind data were scaled to a 3-m height AGL using a logarithmic profile with a
232 specified zero-displacement plane, d , of 0.066 m and a surface roughness, z_0 , of 0.01 m representative of
233 the graded areas around oil and gas areas as used in Bridger's algorithm (Johnson et al., 2021).

234 As in Chen et al. (2022), additional data from internal controlled release studies were provided by
235 Kairos to augment the present analysis of detection probabilities and quantification error/uncertainty. These
236 confidential data include controlled source rate, estimated wind-normalized source rate, measured wind
237 speed, and one-minute gust wind speed from the Dark Sky database for 375 additional non-zero releases.
238 Noting that the blindedness of Kairos' internal studies could not be evaluated, within these data a total of
239 45 releases were missed and 296 releases were automatically detected by Kairos' algorithm; the remaining
240 34 were tagged as partial detects, which required human interpretation to identify a plume. When combined
241 with the publicly available controlled release data of Sherwin et al. (2021) (which are treated as automated
242 detects since the available data did not distinguish partial detects), there were a total of 485 detects, 34
243 partial detects, and 63 missed detections. Additional analysis in the SI shows the effects of treating these
244 data sets separately. For the quantification uncertainty modelling, where only sources greater than 50 kg/h
245 were considered and partial detections were not quantified, and there were total of 148–376 available source
246 measurements depending on which wind data source was considered.

247 **2.4 Published Controlled Release Data for NASA JPL's AVIRIS-NG**

248 A POD function for the AVIRIS-NG sensor was derived using the controlled release data reported by
249 Thorpe et al. (2016). These experiments were originally designed to evaluate the ability of AVIRIS-NG in
250 detecting methane point sources and the available data do not include separate source rate estimates from
251 the plane. A total of 143 non-blinded controlled releases were completed over seven days in June 2013

252 from three separate sites within the Rocky Mountain Oilfield Testing Center in Wyoming, U.S.A. Thorpe
253 et al. (2016) measured wind speeds at 8–9 m AGL using a 3D ultrasonic wind anemometer. For the present
254 analysis of detection probability, reported wind speeds (averaged over the minute preceding a detection)
255 were scaled from an average height of 8.5 m AGL to 3 m AGL using the same logarithmic profile and
256 parameters noted above; the resulting wind speeds at 3 m spanned 0.66-7.5 m/s. Controlled release rates
257 ranged from 2.2 to 96 kg/h and flight altitudes were between 430 to 3800 m AGL. For each release, the
258 methane plume was flagged as either detected (automatic detection by algorithm, N = 94), partially detected
259 (requiring human interpretation, N = 25), or missed (N = 24).

260 **3 Statistical Analysis**

261 **3.1 Generalized Approach to Deriving Robust Probability of Detection Functions**

262 For a specified remote detection technology, the probability of detection (POD) function represents the
263 likelihood of successfully detecting an emitter at some source rate for a given set of conditions during a
264 single measurement observation. Although different technologies may be affected by additional
265 parameters, in general, detectability of a given source (at rate Q) depends on the wind field that drives
266 plume dispersion, the spatial resolution of the measurement, and the effective signal-to-noise ratio (SNR)
267 of the measurement system. For simplicity, the effects of wind can be parameterized by the measured 3-m
268 wind speed (u_3). For Bridger’s GML technology, the measured 3-m wind speed is computed from in-situ
269 wind measurements at 1 Hz using Bridger’s Gaussian smoothing algorithm. For the imaging spectrometers,
270 measured wind speed is averaged over one minute prior to the aircraft overpass to be consistent with
271 Sherwin et al. (2021). For a fixed set of sensor optics, the ground-level spatial resolution is defined by the
272 altitude of the measurement system above ground level (\tilde{h} [m]). The effective SNR for a given
273 measurement is itself a function of Q and u_3 (which affect the observed path-integrated concentration of
274 the plume), \tilde{h} (which affects signal strength through the inverse square law), the spectral albedo of the
275 ground (which affects the strength of the return signal), and potentially other parameters specific to the
276 technology. Although additional SNR data may or may not be readily available for a given technology as
277 further considered below, it is initially considered in this general analysis as a representative scene noise in
278 units of column density (\tilde{n} [ppm-m]). Using these parameters, a POD function can be derived that depends
279 on $\mathbf{x} = [Q, u_3, \tilde{h}, \tilde{n}]^T$. Technically, the plume height (\tilde{z}_p) is also a relevant parameter since plume
280 dispersion is height-dependent; however, since this is undefined for a failed detection, it is necessarily
281 ignored in the derivation of a POD function.

282 A broad range of potential POD functions were evaluated using binary regression on the collected
283 controlled release data. The objective of binary regression is to model a *discrete* binary dependent variable,

284 here D representing a successful (1) or failed (0, “missed”) detection, which follows a Bernoulli distribution
 285 having the POD function, $POD(\mathbf{x})$, as its parameter, i.e.,

$$D \sim \text{Bernoulli}(POD(\mathbf{x})) \quad (1)$$

286 The POD function ($POD(\mathbf{x})$) is modelled as a composite of a “predictor” function ($g(\mathbf{x}; \boldsymbol{\phi})$), with variables
 287 \mathbf{x} and coefficients $\boldsymbol{\phi}$, and a *continuous* “inverse link” function ($F(g(\mathbf{x}; \boldsymbol{\phi}); \boldsymbol{\theta})$), with coefficients $\boldsymbol{\theta}$:

$$POD(\mathbf{x}) \equiv F(g(\mathbf{x}; \boldsymbol{\phi}), \boldsymbol{\theta}) \quad (2)$$

288 For a candidate pair of predictor and inverse link functions, $\boldsymbol{\phi}$ and $\boldsymbol{\theta}$ are obtained by maximum likelihood
 289 estimation (MLE) of the Bernoulli distribution using controlled release data. This can be found via
 290 optimization to minimize ℓ , the negative logarithm of the likelihood function, where for the Bernoulli
 291 distribution:

$$\ell(\boldsymbol{\phi}, \boldsymbol{\theta}) = \sum_i -(D_i \ln F_i + (1 - D_i) \ln(1 - F_i)) \quad (3)$$

292 and $F_i = F(g(\mathbf{x}_i; \boldsymbol{\phi}), \boldsymbol{\theta})$ for each controlled release data point, i .

293 For a fixed probability of detection (p), the POD function may be inverted to define contours of constant
 294 sensitivity for the measurement technique. In the present case, this permits calculation of a critical source
 295 rate at some detection probability, as a function of the remaining parameters in \mathbf{x} – i.e., $Q_p(u_3, \tilde{h}, \tilde{n}; p)$. A
 296 linear prediction model is often used in binary regression, such that $g(\mathbf{x}) = \boldsymbol{\phi}^T \mathbf{x}$, which is coupled with a
 297 logistic inverse link function (logistic regression) or a normal cumulative distribution function (CDF; probit
 298 model). However, in the present application, this approach produces lines of constant detection probability
 299 that converge to zero at zero wind ($u_3 = Q_p = 0$) for a fixed aircraft altitude and scene noise. This implies
 300 that an infinitesimally small emitter could be detected as wind reduces towards zero, which is non-physical
 301 for a noise-laden system. To avoid this, candidate predictor functions are permitted to be nonlinear, while
 302 remaining monotonic with each element in \mathbf{x} and non-negative (consistent with the definition of each
 303 element). Candidate predictor functions are also required to provide a non-negative output that increases
 304 with the likelihood of detection. The inverse link function then maps the output of the predictor function
 305 to a continuous POD between 0 and 1, as required.

306 **3.2 Source Quantification Uncertainty**

307 To interpret estimated source rate data, it is critical that measurement uncertainties are thoroughly
 308 understood. This section presents the method by which controlled release data can be used to derive
 309 predictive estimates for the true source rate (Q) given an estimated source rate (\tilde{Q}). Mathematically, the
 310 objective is to derive the conditional probability of Q given \tilde{Q} – i.e., $\pi(Q|\tilde{Q})$. This challenge was
 311 approached by parsing observed errors during controlled release experiments into bias and precision
 312 components.

313 Consider hypothetical multiple detections/measurements of a single, steady-state source observed on a
 314 single, specific date. It can be assumed that, *on average*, there will be some error in the estimated value of
 315 the source rate, which represents *bias* in the measurement of this source on the specific date. A bias-
 316 correction procedure that accounts for this average error in \tilde{Q} can be developed using a *bias-corrected*
 317 estimate of the source rate ($\hat{Q} = f_B(\tilde{Q})$), which may be assumed to follow a conditional distribution
 318 $\pi(\hat{Q}|\tilde{Q})$. A *precision distribution* that accounts for precision error of the bias-corrected estimate can be
 319 similarly defined, $\pi(Q|\hat{Q})$. The desired distribution of the true source rate given the estimated source rate
 320 can then be computed from these distributions via:

$$\pi(Q|\tilde{Q}) = \int_{\hat{Q}} \pi(Q|\hat{Q}) \pi(\hat{Q}|\tilde{Q}) d\hat{Q} \quad (4)$$

321 where the integration is performed over all possible values of \hat{Q} . For convenience, Eq. (4) can be re-written
 322 in terms of *probabilistic* correction parameters κ_Q and λ_Q – where $\kappa_Q = \hat{Q}/f_B(\tilde{Q})$ is a bias-correction
 323 parameter and $\lambda_Q = Q/\hat{Q}$ is a precision-correction parameter – that are *statistically independent* from \tilde{Q} , \hat{Q} ,
 324 and Q . Letting the probability distributions of these correction parameters be $\pi_{\kappa_Q}(\kappa_Q)$ and $\pi_{\lambda_Q}(\lambda_Q)$,
 325 respectively, their statistical independence implies via a change of variables that $\pi(Q|\hat{Q}) \equiv \pi_{\lambda_Q}(Q/\hat{Q})/\hat{Q}$
 326 and $\pi(\hat{Q}|\tilde{Q}) \equiv \pi_{\kappa_Q}(\hat{Q}/f_B(\tilde{Q}))/f_B(\tilde{Q})$. Introducing these into Eq. (4) gives:

$$\pi(Q|\tilde{Q}) = \int_{\hat{Q}} \pi_{\lambda_Q}\left(\frac{Q}{\hat{Q}}\right) \pi_{\kappa_Q}\left(\frac{\hat{Q}}{f_B(\tilde{Q})}\right) \frac{1}{\hat{Q} f_B(\tilde{Q})} d\hat{Q} \quad (5)$$

327 Since bias-correction accounts for the average error in \tilde{Q} , the parameters of the precision-correction
 328 distribution (π_{λ_Q}) must be chosen to yield a unit mean. Likewise, the parameters of the bias-correction

329 distribution (π_{κ_Q}) can be constrained to have a unit mean to permit consideration of measurement bias
330 through the optimized coefficient(s) of the bias-correction function (f_B).

331 There is one simplifying limiting case for the conditional distribution shown in Eq. (5) that is necessary
332 if controlled release data are constrained to a small set of sites and/or measurement days. In this case,
333 measurement error must be assumed to be *independent* of time and location, implying that the required
334 bias-correction is non-probabilistic. With this assumption, Eq. (4) simplifies to:

$$\pi(Q|\tilde{Q}) = \pi_{\lambda_Q} \left(\frac{Q}{f_B(\tilde{Q})} \right) \frac{1}{f_B(\tilde{Q})} \quad (6)$$

335 The conditional probability distributions in Eq. (6) were computed via MLE using controlled release data
336 for Bridger’s GML and Kairos’ LeakSurveyor technology. This approach optimizes the parameters for π_{λ_Q}
337 (constrained to yield a unit mean) and the coefficients of the bias-correction function, f_B .

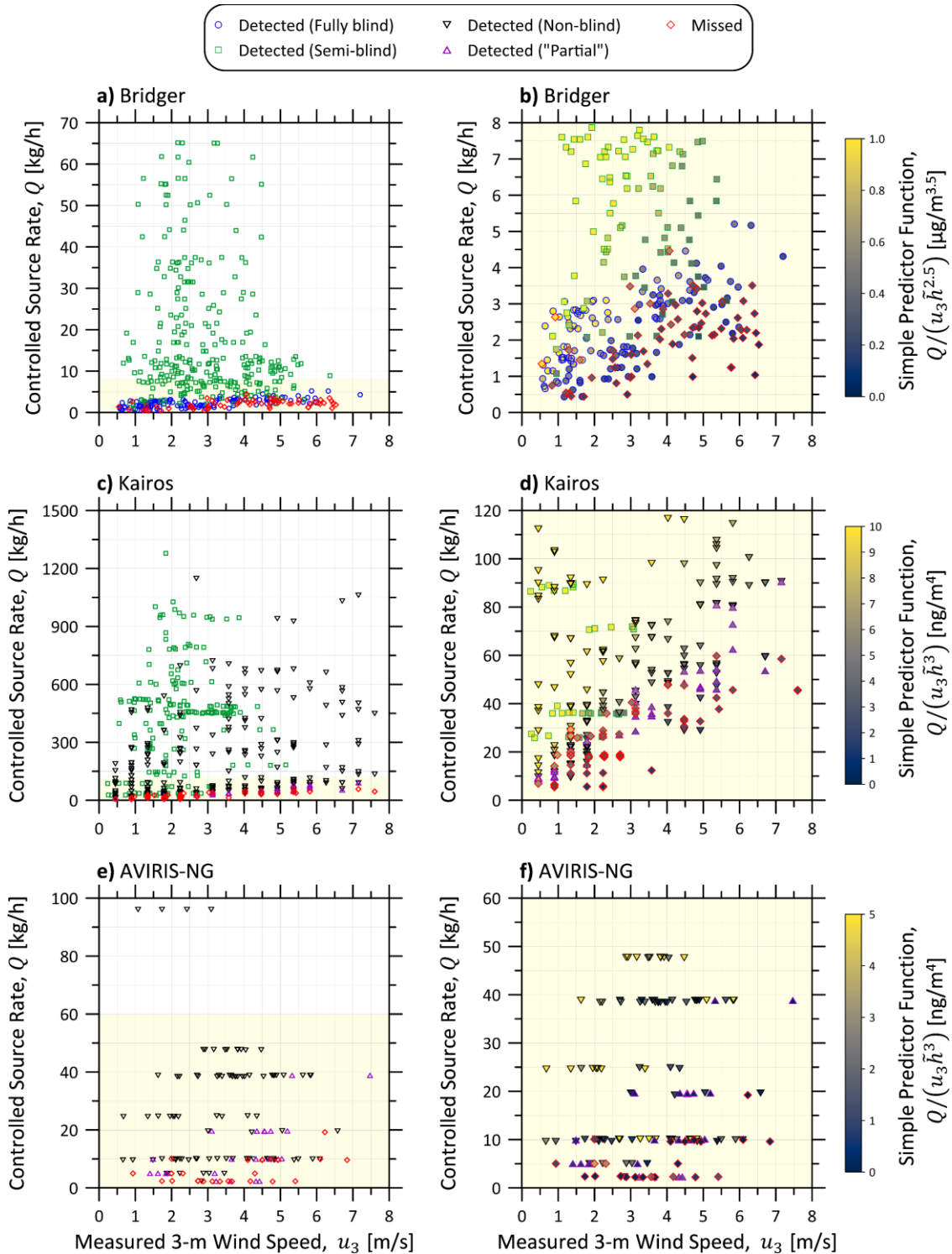
338 Myriad other parameters could influence error in source rates estimated from aerial measurements.
339 These include the time-history of the turbulent wind field over the site as well as parameters impacting the
340 quality of the measurement signal (e.g., aircraft altitude/orientation and surface albedo). In the most general
341 sense, the desired probability distribution(s) should be conditioned on these additional parameters.
342 However, error caused by these parameters are likely to be highly site-, source-, and time-dependent, such
343 that these confounding variables are inherently considered if extensive controlled release data for multiple
344 sites over multiple days are available and Eq. (5) can be used to model quantification error. Conversely,
345 since Eq. (6) assumes errors are independent of site, source, and time, this latter model can be expected to
346 underestimate variance in the quantification error. Sufficient data were obtained during the high-flowrate
347 controlled release experiments of Bridger’s GML to permit evaluation of quantification error via both Eq.
348 (5) and (6). This case study identifies the importance of site- and day-dependent quantification error is
349 discussed in Section 4.2.1 below.

350 **4 Results**

351 ***4.1 Probability of Detection***

352 Starting first with the detailed case-study of Bridger’s GML, Figure 1a plots the 466 non-zero controlled
353 releases obtained during the 2020 and 2021 campaigns as a function of measured 3-m wind speed,
354 calculated from in-situ measurements following Bridger’s Gaussian smoothing algorithm. Successful
355 detections of fully and semi-blinded releases are identified in blue and green, respectively, and misses in

356 red. There were no false positives during the 29 zero controlled releases. Over this range of wind speeds
357 between 0.5 and 7.2 m/s, all controlled release sources greater than ~4.5 kg/h were detected. Figure 1b
358 shows a magnified view of the same data for source rates less than 8 kg/h, which highlights the probabilistic
359 nature of detection success.



360

361 **Figure 1: Available controlled release data for (a,b) Bridger Photonics GML, (c,d) Kairos LeakSurveyor, and**
 362 **(e,f) AVIRIS-NG. Successful detections are outlined in blue (fully blinded data), green (semi-blinded data),**
 363 **or black (non-blinded data); partial detections in purple; and missed detections in red. Righthand panels (b,**
 364 **d, and f) show a zoomed subset of lower release rate data from the corresponding left panels, where the data**
 365 **points are also shaded according to each technique's simple predictor function (described in the main text) as**
 366 **outlined on the right of each panel.**

367 Expectedly, successful detection appears more likely at higher source rates and lower wind speeds –
 368 i.e., detection probability is correlated with the wind-normalized source rate as in previous studies (e.g.,
 369 Sherwin et al., 2021). This is anticipated by the simplified Gaussian plume dispersion model (Hanna et al.,
 370 1982), where the wind-normalized source rate is proportional to the plume column density along the vertical
 371 axis (i.e., the observable “signal” for an airborne measurement). However, detection is also affected by the
 372 strength of the return signal at the optics which is proportional to \tilde{h}^{-2} (inverse square law) and the spatial
 373 resolution of the imagery, which for Bridger’s scanning laser and GML optics is approximately proportional
 374 to $\tilde{h}^{-0.5}$. Including these effects, while still ignoring the effect of instrument noise for the time-being,
 375 provides an informative, non-parametric, *simple* predictor function for Bridger’s GML, $g(\mathbf{x}; \Phi) \approx \frac{Q}{u_3 \tilde{h}^{2.5}}$.
 376 This function is used to colour the data in Figure 1b, scaled to units of $\mu\text{g}/\text{m}^{3.5}$. Visually, the colour gradient
 377 in the data from the top-left (high detection probability) to the bottom right (low detection probability)
 378 suggests strong correlation of this simple predictor with detectability.

379 Similar data are shown for the Kairos LeakSurveyor (Figure 1c-d) and AVIRIS-NG (Figure 1e-f)
 380 instruments. In contrast to Bridger’s GML with actively scanning optics, the detection sensitivity of these
 381 passive imaging spectrometers is expectedly lower, such that some emissions likely to be detected by
 382 Bridger may be missed by Kairos’ LeakSurveyor or AVIRIS-NG. Additionally, for these imaging optics
 383 that can be approximated with a pinhole model, spatial resolution at the ground/plume is linear with aircraft
 384 altitude, implying that signal strength is proportional to \tilde{h}^{-1} . Combining this with the inverse square law
 385 (\tilde{h}^{-2}) suggests that the equivalent *simple* prediction function these techniques should be $g(\mathbf{x}; \Phi) \approx \frac{Q}{u_3 \tilde{h}^3}$,
 386 indicating a greater sensitivity to aircraft altitude than Bridger’s GML. Figure 1d and f show the controlled
 387 release data according to this latter predictor function in units of ng/m^4 – recall however, that available
 388 Kairos data were acquired at the single targeted altitude of 900 m AGL. Interestingly, in contrast to
 389 Bridger’s GML, the gradient in this colouring scheme is less pronounced for AVIRIS-NG, indicating that
 390 detection sensitivity is not well-captured by the simple predictor model.

391 Although potentially useful, the simple predictor functions $g(\mathbf{x}; \Phi) \approx \frac{Q}{u_3 \tilde{h}^{2.5}}$ and $g(\mathbf{x}; \Phi) \approx \frac{Q}{u_3 \tilde{h}^3}$ in
 392 Figure 1b, d, and f are sub-optimal since, in addition to being non-parametric and approximate, this
 393 formulation forces contours of constant POD to be linear and converge at the origin in the Q - u_3 domain.
 394 Thus, for a fixed aircraft altitude, this formulation results in the same non-physical POD at low wind speeds
 395 as the linear predictor model. To avoid this issue and to generalize the predictor model, the present analysis
 396 considers an optimizable model of the form:

$$g(\mathbf{x}; \boldsymbol{\phi}) = \phi_7 \frac{(Q_{[\text{kg/h}]} - \phi_1)^{\phi_3}}{\tilde{n}_{[\text{ppm}\cdot\text{m}]}^{\phi_4} \left(\frac{h_{[\text{m}]}}{1000}\right)^{\phi_5} \left(u_{3[\text{m/s}]} - \phi_2\right)^{\phi_6}} \quad (7)$$

397 where representative scene noise (\tilde{n}) has been introduced for completeness and may be optionally
 398 considered via optimization of coefficient ϕ_4 and units of each variable have been explicitly stated in square
 399 brackets. Choosing $\phi_1 > 0$ and/or $\phi_2 < 0$ ensures a physically reasonable POD at zero-wind, unlike the
 400 linear prediction model and the simple, non-parametric predictor functions described above and used to
 401 colour data in Figure 1b, d, and f. Similarly, non-negative exponents ϕ_{3-6} allow for deviation from
 402 linearity or, in the case of ϕ_5 for aircraft altitude, from the simple predictor functions described above.
 403 Importantly, the generalized predictor model of Eq. (7) is non-negative and monotonically increases with
 404 source rate and decreases with scene noise, aircraft altitude, and 3-m wind speed. This means that candidate
 405 inverse link functions can take the form of the cumulative distribution function (CDF) of any distribution
 406 with non-negative support (e.g., lognormal, Fréchet, etc.).

407 As further detailed in the SI (see especially Table S1), the optimization considered a broad range of
 408 possible inverse link functions while independently testing the importance of each variable in Eq. (7).
 409 Considering first the subset of controlled release measurements where scene noise data were available, in
 410 all instances the optimization showed that including either scene noise *or* aircraft altitude in the model, i.e.,
 411 permitting ϕ_4 *or* ϕ_5 to be non-zero, was strongly statistically justified. By contrast, including both
 412 parameters was either not justified or only marginally justified ($\Delta AICc < \sqrt{10}$, see SI); that is, classed as
 413 “not worth more than a bare mention” (Kass and Raftery, 1995; Snipes and Taylor, 2014). Thus, given that
 414 aircraft altitude is a trivial parameter to quantify (and in the present case available for Bridger’s GML as a
 415 standard output), the remainder of the POD derivation ignores scene noise, forcing $\phi_4 = 0$ and optimizing
 416 for the exponent on aircraft altitude, ϕ_5 .

417 Subsequent optimization was performed using all available controlled release data plotted in Figure 1a
 418 for Bridger’s GML (N = 466), Figure 1c for Kairos’ LeakSurveyor (N = 582), and Figure 1f for AVIRIS-
 419 NG (N = 139). As an example, the best-fitting model for the GML data had the following optimized
 420 predictor function:

$$g(Q, u_3, \tilde{h}) = \frac{0.152 Q_{[\text{kg/h}]}^{1.07}}{\left(\frac{\tilde{h}_{[\text{m}]}}{1000}\right)^{2.44} (u_{3[\text{m/s}]} + 2.14)^{1.69}} \quad (8)$$

421 and employed a Fréchet CDF for the inverse link function:

$$F(g) = \exp(-0.372g^{-2.53}) \quad (9)$$

422 Combined, these give the probability of detection for any specific source rate, wind speed, and altitude
 423 using Bridger's GML. Importantly, the generalized approach used to produce this detailed model can be
 424 readily extended to any other technology for which sufficient controlled release data are available. Using
 425 published controlled release data for Kairos' LeakSurveyor (Sherwin et al., 2021) and AVIRIS-NG (Thorpe
 426 et al., 2016) and additional internal controlled release data from Kairos, POD functions were derived for
 427 each of these technologies using the developed method. The final optimized POD functions, which
 428 combine the predictor and inverse link functions, are summarized for each technology in Table 2; optimized
 429 predictor functions are available in the SI. For both Kairos' LeakSurveyor and AVIRIS-NG cases,
 430 representative instrument noise data for the controlled releases were not available (hence, $\phi_4 = 0$).
 431 Additionally, for Kairos' LeakSurveyor, aircraft altitude was constant during controlled release
 432 experiments so the optimized exponent on aircraft altitude (ϕ_5) was also necessarily ignored.

433
434
435

Table 2: Derived POD functions for GML, LeakSurveyor, and AVIRIS-NG, combining optimized predictor and inverse link functions. Detailed equations of the predictor and inverse link functions for each technology are summarized in Table S2 of the SI.

Technology	Optimized Probability of Detection (POD) Function
Bridger Photonics Inc. Gas-mapping LiDAR (GML)	$\text{POD} = \exp \left(- \left(\frac{0.224 Q_{[\text{kg/h}] }^{1.07}}{\left(\frac{\tilde{h}[\text{m}]}{1000} \right)^{2.44} (u_3[\text{m/s}] + 2.14)^{1.69}} \right)^{-2.53} \right)$
Kairos Aerospace LeakSurveyor ^a (Excluding Partial Detections)	$\text{POD} = 1 - \left(1 + \left(\frac{(8.50 \times 10^{-3}) Q_{[\text{kg/h}] }^{1.99}}{(u_3[\text{m/s}] + 0.534)^{1.92}} \right)^2 \right)^{-1.5}$
Kairos Aerospace LeakSurveyor ^a (Including Partial Detections)	$\text{POD} = 1 - \left(1 + \left(\frac{(7.71 \times 10^{-3}) Q_{[\text{kg/h}] }^{1.87}}{(u_3[\text{m/s}])^{1.41}} \right)^2 \right)^{-1.5}$
NASA JPL AVIRIS-NG (Excluding Partial Detections)	$\text{POD} = 1 - \left(1 + \left(\frac{(31.1 \times 10^{-3}) Q_{[\text{kg/h}] }^{1.99}}{\left(\frac{\tilde{h}[\text{m}]}{1000} \right)^{1.91} \exp(0.239 u_3[\text{m/s}])} \right)^2 \right)^{-1.5}$
NASA JPL AVIRIS-NG (Including Partial Detections)	$\text{POD} = \exp \left(- \left(\frac{0.365 Q_{[\text{kg/h}] }^{1.10}}{\left(\frac{\tilde{h}[\text{m}]}{1000} \right)^{0.731} \exp(0.114 u_3[\text{m/s}])} \right)^{-2.53} \right)$

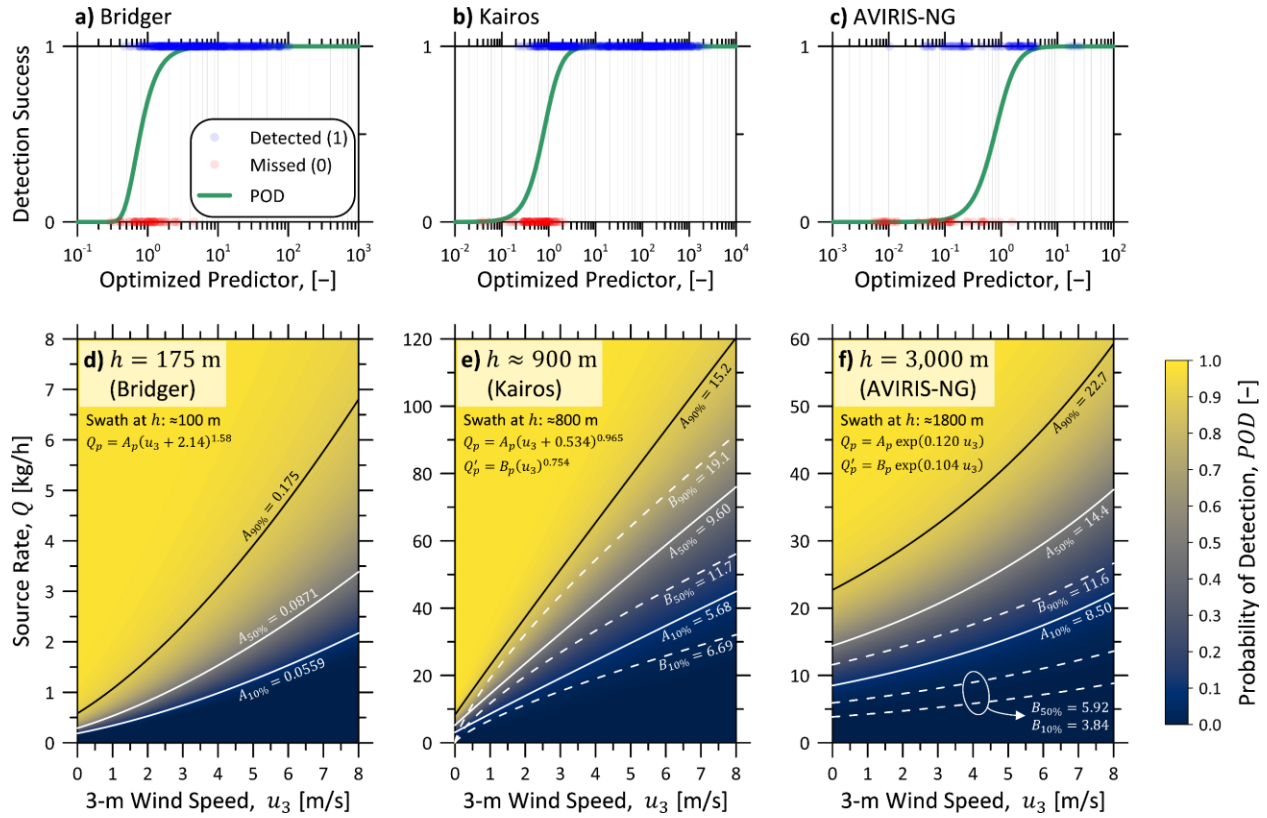
^a Aircraft altitude during controlled release experiments of Kairos' LeakSurveyor did not deviate from the targeted aircraft altitude of 900 m AGL (approximately 3000 ft), so aircraft altitude is necessarily ignored in the stated POD function. The optimized model can theoretically be extended to other altitudes by forcing the exponent on aircraft altitude to its expected value of 3.0 and updating other coefficients as necessary. Note however that there are no public data to support model accuracy at other altitudes and this extrapolation should be performed with caution given the observed deviation of AVIRIS-NG's optimized predictor function from the same expected value of 3.0.

436

437 Optimization of the generalized predictor function in Eq. (8) using the controlled release data for
438 Bridger's GML technology identified an optimal exponent on aircraft altitude (ϕ_5) of 2.44, quite close to
439 the theoretical/expected value of 2.5. By contrast, optimization of the AVIRIS-NG controlled release data
440 yielded an optimal exponent on aircraft altitude of 0.731–1.91, which is lower than the expected value of
441 3.0 assuming simple pinhole optics. Given this deviation and noting that aircraft altitude was not varied

442 from the targeted level in the controlled release studies of Kairos' Leak Surveyor, one should use caution
443 if seeking to extrapolate from the presented POD function for Kairos to other altitudes.

444 Figure 2a-c plots detection success against the value of the optimized predictor function for the
445 controlled releases of Bridger's GML, Kairos' LeakSurveyor, and AVIRIS-NG, respectively. The
446 optimized inverse link function is overlaid in each plot. Figure 2d-f combines the optimized predictor and
447 inverse link to display the POD function within the $Q-u_3$ domain at typical/common aircraft altitudes for
448 Bridger's GML (175 m), Kairos' LeakSurveyor (900 m), and AVIRIS-NG (3000 m, Duren et al., 2019;
449 Thorpe et al., 2021), respectively. Contours at probabilities of detection of 10, 50, and 90% – and the
450 associated functions, Q_p – are also plotted as solid lines. The dashed lines (and associated functions, Q'_p)
451 show the POD if partial (human-identified) detections are included in the analyses of Kairos' LeakSurveyor
452 and AVIRIS-NG and treated equally as algorithmic detections.



453
 454 **Figure 2: Robustly derived probability of detection (POD) functions for Bridger's GML technology, Kairos'**
 455 **LeakSurveyor technology, and AVIRIS-NG. a-c) detection success against optimized predictor function**
 456 **values for all available controlled release data for each instrument alongside the corresponding optimized**
 457 **inverse link function (green line). d-f) calculated probability of detection as a function of source rate and 3-m**
 458 **wind speed at typical flight altitudes (corresponding approximate swath widths also shown) for each**
 459 **instrument. Contours for probabilities of detection of 10, 50, and 90% and their associated functions (Q_p) are**
 460 **overlaid in each plot as solid lines. For comparison, POD contours if partial detections are included are also**
 461 **plotted with their associated functions (Q'_p) as dashed lines. Table 2 provides general equations for POD as a**
 462 **function of source rate, wind speed, and altitude (where relevant) for all cases in this figure.**

463 The POD functions plotted in Figure 2d-f and summarized in Table 2 provide continuous detection
 464 probabilities on a *measurement-specific* basis for any given wind speed, source rate, and altitude. These
 465 functions have not existed to date and are precisely what is required for realistic analysis using emissions
 466 abatement simulators like FEAST (Kemp et al., 2016) and modelling efforts supporting alt-FEMP
 467 applications. In FEAST for example, detection sensitivity has to date been treated as a binary variable with
 468 successful detection assumed if an instrument's sensitivity is exceeded by the maximum plume
 469 concentration estimated from Gaussian plume dispersion theory. This approach inherently ignores the
 470 continuous nature of detection probability and assumes idealized plume dispersion that is not supported by
 471 the data. The continuous POD functions developed in this work identify non-linear sensitivities to source
 472 rate size and measurement conditions and can be readily implemented within FEAST and other models to

473 probabilistically assess detection success. Similarly, robust POD data are vital for objective analysis of
474 missed detections in situations where multiple measurements are made over the same facility.

475 As expected, and noting the different scales in Figure 2d-f, the detection sensitivities of Bridger's active
476 sensor are much lower than either of the passive sensors. Considering typical altitudes of 175, 900,
477 and 3000 m AGL (corresponding to approximate measurement swaths of 100, 800, and 1800 m) for each
478 technology respectively, at a common reference wind speed of 3 m/s, the controlled release data identify
479 that Bridger's GML might be expected to detect single sources of 1.2 kg/h in size at 50% probability, Kairos
480 a 27/32 kg/h source, and AVIRIS-NG a 8.1/21 kg/h source (the latter two lower/upper values depending on
481 whether partial, human-reviewed detections are considered as detections or not). At 90% detection
482 probability, these thresholds become 2.3 kg/h, 44/51 kg/h, and 16/33 kg/h, respectively. At an aircraft
483 altitude of 8000 m AGL, the upper limit of flights in a recent study (Thorpe et al., 2021), the 50% and 90%
484 detection thresholds for AVIRIS-NG are 15/53 kg/h and 30/84 kg/h, respectively, although estimates for
485 this altitude are necessarily extrapolated from the available published data which includes releases for flight
486 altitudes up to 3800 m AGL. At fixed altitudes, the optimized POD functions for all three technologies
487 provide physically realistic non-zero intercepts at zero wind speed when ignoring partial detections. These
488 contours contrast with assumed detection sensitivities or partial detection ranges with non-physical zero-
489 intercepts based on wind-normalized source rates for Kairos' LeakSurveyor (Berman et al., 2021; Chen et
490 al., 2022; Sherwin et al., 2021) as well as the assumed linear model of Johnson et al. (2021) for Bridger's
491 GML. Figure S4 of the SI compares the newly derived continuous POD functions with these previously
492 published detection sensitivities for each technology. There is a slight improvement in the detection
493 sensitivity of Bridger's GML over that estimated from limited tests in the 2019 data of (Johnson et al.,
494 2021). Detection sensitivities are of similar magnitude for Kairos' LeakSurveyor as in Sherwin et al.'s
495 (2021) and Berman et al.'s (2021) analyses. Likewise, the present approach overlaps significantly with
496 Thorpe et al.'s (2016) stated partial detection range, however the new result improves upon this by
497 parameterizing the POD with wind speed and altitude aircraft.

498 The optimized POD function for Kairos' LeakSurveyor is approximately linear with wind speed when
499 ignoring partial detections. While this result is justified by goodness-of-fit statistics, subjective
500 inclusion/exclusion of data can yield significantly different results. Using this technology as an example
501 and referring to Figure S5 in the SI, POD contours are strongly super-linear if Sherwin et al.'s (2021) data
502 are considered alone (Figure S5a) but, by contrast, become approximately linear if only Kairos' internal
503 data are considered (Figure S5b). When combining these unique data sets, the optimized POD function
504 biases towards the former and yields contours that are approximately linear (Figure 2e and S5c). This
505 sensitivity to data inclusion is likely due to the scarcity of data near the sensitivity limit in Sherwin et al.'s

506 (2021) experiments (see Figure S5a in the SI). For instance, one-minute-averaged 3-m wind speeds during
507 Sherwin et al.'s (2021) experiments did not exceed 5.5 m/s as compared to maximum wind speeds of 7.4 m/s
508 in the Bridger GML and >8.0 m/s in the AVIRIS-NG controlled release data. Moreover, due to
509 instrumentation constraints noted by Sherwin et al. (2021), releases near the sensitivity limit were
510 occasionally held constant during consecutive (up to 16) flight passes, letting the variable wind perturb
511 detectability of the plume. Consequently, the available controlled release data tend to be clustered in the
512 Q - u_3 domain, such that a POD function for Kairos' LeakSurveyor derived from Sherwin et al.'s (2021) data
513 alone should not be extrapolated. Nevertheless, the observed sensitivity of the optimized POD function to
514 the contributing datasets supports the continued acquisition (and public sharing) of controlled release data
515 for these technologies.

516 The controlled release data for AVIRIS-NG resulted in optimized POD functions with large values of
517 ϕ_2 . This coefficient, which translates the wind speed coordinate in the predictor and POD functions,
518 optimized toward negative infinity as ϕ_1 and ϕ_6 optimized toward positive infinity. It is unclear whether
519 this is a consequence of the plume segmentation algorithm employed by Thorpe et al. (2016) or their
520 experimental approach to the controlled releases. Given this result, at the optimum, the predictor function
521 for the AVIRIS-NG instrument can be more concisely written than Eq. (7) by replacing $(u_3 - \phi_2)^{\phi_6}$ with
522 $\exp(\phi_2' u_3)$ as shown in the final optimized POD functions of Table 2. This formulation avoids potential
523 issues with numerical resolution and improves convergence during optimization. Considering this specific
524 observation, but also the POD analysis more generally, it is important to note that optimized coefficients
525 are fundamentally empirical in nature; caution should be used in interpreting/comparing fitted coefficients,
526 which are sensitive not just to the underlying data, but also the specific form of the best-fitting predictor
527 and inverse link functions identified for each technology.

528 As presented, the derived POD assumes accurate knowledge of aircraft altitude and 3-m wind speed.
529 This is the appropriate form when trying to understand what might be detectable in a range of field study
530 scenarios and/or modelling of alternate fugitive emissions management programs (Alt-FEMP) or
531 alternative means of emission limitation (AMEL) proposals. However, when interpreting data from a
532 specific field campaign, accurate in-situ wind data are generally not available and database/modelled wind
533 speed at some arbitrary height above ground level (z) must instead be used to infer the POD. This scenario
534 necessarily requires an error model for the wind speed and, if $z \neq 3$ m, an assumed vertical wind speed
535 profile. Such a model is likely to be highly dependent on time and location as well as the source of the
536 wind speed estimate and ideally should be derived from data relevant to any particular measurement
537 campaign. However, if a wind error model of the form $\pi(u_3|\tilde{u}_z)$ exists (i.e., a conditional distribution of

538 the true 3-m wind speed given the available estimate at z – i.e., \tilde{u}_z), then the POD can be readily quantified
 539 considering bias/precision in the estimated wind speed via:

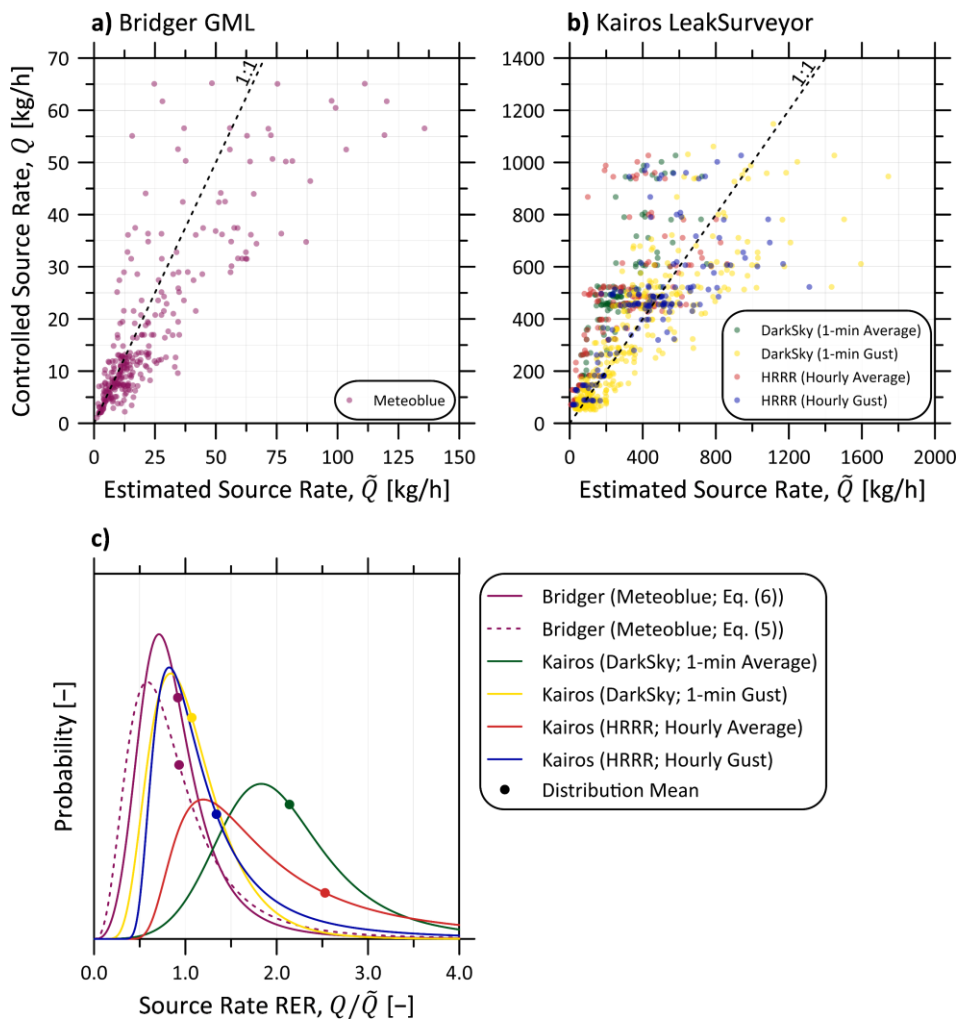
$$\text{POD}(Q, \tilde{u}_z, \tilde{h}) = \int_0^{\infty} \text{POD}(Q, u_3, \tilde{h}) \pi(u_3 | \tilde{u}_z) du_3 \quad (10)$$

540 Wind speed error distributions from a reference 3-m height $\pi(u_3 | \tilde{u}_3)$, were derived using available wind
 541 data from the controlled release trials of Bridger’s GML and Kairos’ LeakSurveyor. The resulting
 542 distributions, optimized in the same manner as the quantification error distributions, are summarized in
 543 Table S4 of the SI and can be used with the optimized POD functions in Table 2 to compute probabilities
 544 of detection given *estimated* wind speed via Eq. (10).

545 **4.2 Source Quantification Uncertainty**

546 Figure 3a and b compare the known (Q) and estimated (\tilde{Q}) source rates across the controlled release studies
 547 of Bridger’s GML and Kairos’ LeakSurveyor technologies. Estimated source rates for Bridger’s GML
 548 technology were taken directly from their reported results; all 284 non-zero, semi-blinded, high-flowrate
 549 releases in the 2020 and 2021 campaigns are shown in Figure 3a alongside a 1:1 parity line. Figure 3b plots
 550 similar data from Sherwin et al.’s (2021) external controlled release experiments and Kairos’ internal
 551 experiments of its LeakSurveyor, where data correspond to all detected controlled releases greater than
 552 50 kg/h and without any identified quality control concerns. Source rates were computed from Kairos’
 553 estimated wind-normalized source rates and multiplied by modelled wind speed at 3-m height above
 554 ground. Four datasets are shown in Figure 3b corresponding to wind data from Dark Sky – one-minute
 555 average (green) and gust (yellow) – and HRRR – one-hour average (red) and gust (blue). Recognizing that
 556 quantification errors scale with source rate, Figure 3c plots the resulting probability distributions for the
 557 *relative* error ratio ($\text{RER} = Q/\tilde{Q}$) from the data in Figure 3a and b according to Eq. (6), which ignores
 558 potential site-to-site and day-to-day variability in measurement accuracy; means of each distribution,
 559 representing overall measurement biases, are identified by points. Bridger’s GML estimates using
 560 Meteoblue wind data and Kairos’ LeakSurveyor estimates using one-minute *gust* data from Dark Sky show
 561 minimal bias errors, with relative error ratios of 0.92 and 1.07, respectively. By contrast, bias errors can be
 562 larger (1.34) when using one-hour gust wind data from HRRR and prohibitively large using one-minute
 563 *average* Dark Sky or one-hour *average* HRRR data (2.14 and 2.53, respectively) with Kairos’
 564 LeakSurveyor technology. Table 3 summarizes key statistics (mean, median, and 95% equal tail confidence
 565 intervals) for each of these distributions shown in Figure 3c and Table S3 of the SI provides detailed
 566 equations for the conditional probability distribution, $\pi(Q|\tilde{Q})$, for each combination of technology and

567 wind speed data source. These distributions are the essential inputs for Monte Carlo methods enabling
 568 comprehensive uncertainty analysis in large measurement campaigns that specifically include aggregation
 569 of detected sources to develop measurement-based inventories (e.g., Tyner and Johnson, 2021).
 570 Importantly, such measurement campaigns may also include multi-pass measurements of single
 571 sources/facilities; the presented distributions can be used to predict and calculate quantification
 572 uncertainties to support survey design and data analysis in this multi-pass context. Using Bridger's GML
 573 as an example, the quantification error model via Eq. (6) suggests the 95% equal tail confidence interval of
 574 the RER for a single pass is 0.31-2.13, which narrows to 0.56-1.52 after just four flight passes.



575
 576 **Figure 3: Summary of controlled release data and quantification error analysis for a) Bridger's GML**
 577 **technology using Meteoblue wind data (purple) and b) Kairos' LeakSurveyor technology, computed using**
 578 **Dark Sky one-minute average (green) and gust (yellow) and HRRR hourly average (red) and gust (blue) wind**
 579 **data. (c) Resulting distributions of the source rate relative error ratio (RER) for each technique and wind**
 580 **source via fitting of Eq. (6) in addition to the source rate RER for Bridger's GML technology using Eq. (5).**
 581 **Distribution means, representing quantification bias error are identified for each distribution by a point.**

582 **Table 3: Statistics of the relative error ratio ($RER = Q/\tilde{Q}$) for Bridger’s GML and Kairos’**
583 **LeakSurveyor technologies; source data corresponds to the high-flowrate (1-66 kg/h) controlled**
584 **releases from the present study and all valid controlled releases > 50 kg/h from Sherwin et al.**
585 **(2021) and Kairos’ internal experiments. RER statistics (mean, median, and 95% equal tail**
586 **confidence interval (CI)) are shown for each technique and, for Kairos’ LeakSurveyor, when using**
587 **different sources of wind speed data.**

Instrument	Wind Source	Wind Statistic	Mean (Bias)	Median	95% Equal Tail CI
Bridger GML	Meteoblue	Proprietary	0.92	0.82	0.31 – 2.13
Kairos LeakSurveyor	Dark Sky	1-min Gust	1.07	0.99	0.45 – 2.17
		1-min Average	2.14	1.99	0.94 – 4.23
	HRRR	1-hr Gust	1.34	1.07	0.57 – 3.74
		1-hr Average	2.53	1.74	0.77 – 8.82
	In Situ	1-min Gust	0.99	0.92	0.45 – 1.88
		1-min Average	1.38	1.29	0.60 – 2.74

588

589 The improved quantification accuracy when using *gust* instead of *average* wind speeds to estimate
590 source rate with Kairos’ LeakSurveyor is somewhat counterintuitive since average wind speed is more
591 indicative of the history of plume propagation prior to any observation. This seemingly anomalous
592 observation could be a result of the coarse spatiotemporal resolution in database/modelled winds, which
593 might tend to underestimate averages of non-negative and right-skewed wind speeds. However, this is
594 much more likely related to how Kairos’ wind-normalized source rate is estimated based on a defined “core”
595 of the plume. Specifically, Kairos estimates wind-normalized source rate by dividing the total observed
596 excess methane mass in the “core” of the plume by the length of this plume “core” in the direction of the
597 wind; to then estimate source rate, this parameter is multiplied by the estimated wind speed. This is
598 equivalent to averaging the flux of methane through control surfaces orthogonal to and spanning the length
599 of the plume core. This approach is only valid in the case of infinite sensitivity where excess methane at
600 the edges of the plume is fully resolved. In practice though, finite sensitivity implies that the excess mass
601 of methane in the plume is inherently underestimated, and this effect is accentuated by constraining the
602 analysis to an arbitrary plume core. To overcome this underestimation of plume mass, an upward correction
603 to wind speed would be necessary. This same result has been identified for satellite-based methane
604 detection methods – particularly the cross-sectional flux (CSF) method (e.g. Varon et al., 2018 and
605 references therein), which is similar to Kairos’ approach. Robust analyses of this quantification method in
606 the context of satellite remote sensing confirms that database/modelled average wind speeds must be
607 calibrated/corrected to accurately recover known source rates. The calibration correction has been found
608 to be sensor noise- and plume-dependent and studies have estimated it to range from +30 to +75% for
609 satellite instruments (Jervis et al., 2021; Varon et al., 2020). Recognizing that database/modelled wind

610 speeds are inherently biased and uncertain, it is possible and perhaps likely that the upward correction used
611 to estimate gust wind speed from an average wind speed tends to mimic this required calibration correction.

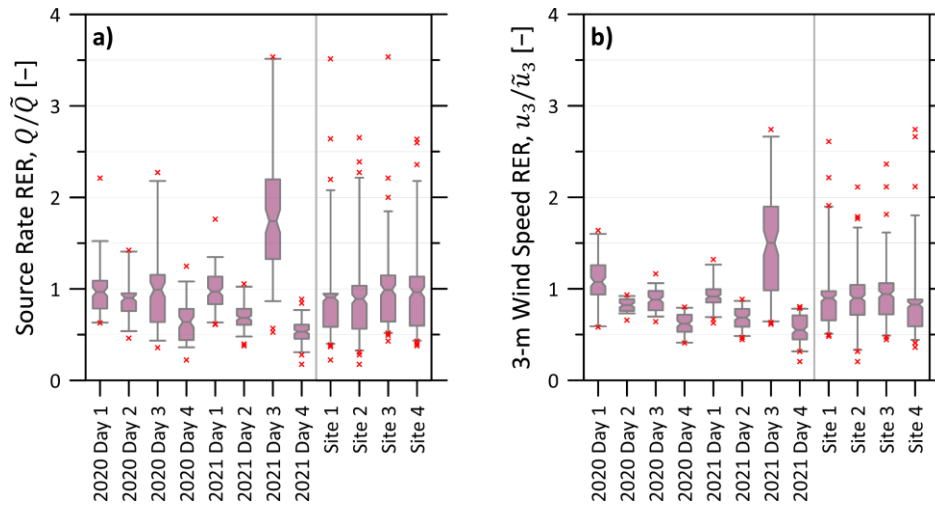
612 To explore this further, Table 3 shows RER statistics for Kairos' LeakSurveyor using in-situ wind speed
613 data from Sherwin et al. (2021) and Kairos' internal controlled release studies. One-minute-averaging of
614 in-situ wind speed tends to underestimate the true source rate (RER of 1.38), corresponding to a +38%
615 calibration correction needed to minimize bias; this is consistent with published corrections needed for
616 satellite imagery using the CSF method (Jervis et al., 2021; Varon et al., 2020). However, the in-situ, one-
617 minute gust wind speed compensates for this underestimation (RER of 0.99). Thus, in this specific
618 example, if wind-normalized source rate is derived using Kairos' plume "core", then the one-minute gust
619 wind speed empirically minimizes bias.

620 *4.2.1 Spatiotemporal Variability of Measurement Bias*

621 Use of the simpler error model shown in Eq. (6) assumes that site-to-site and day-to-day bias in
622 measurement error for a given technique is negligible. While this is a necessary assumption if controlled
623 release data are limited to few locations/days, it is also simplistic. For example, drift in optical components
624 and general atmospheric conditions may influence day-to-day variability in quantification accuracy, while
625 localized conditions such as wind direction/turbulence and ground albedo can affect site-to-site variability.
626 To glean insight into this bias variability, an additional analysis was performed using the present controlled
627 release data for Bridger's GML technology, which includes releases from four oil and gas sites recorded
628 over multiple days in two field campaigns one year apart. Figure 4a presents a box-whisker diagram for
629 the relative error ratio (RER) of the Bridger GML-estimated source rate, which takes the 284 controlled
630 releases and computes statistics for data aggregated by measurement day (eight days spanning 2020 and
631 2021) and site (four locations). In these diagrams the central bar represents the interquartile range (25th to
632 75th percentile), the gray bars extend to the 90% equal tail confidence interval (CI), and the red crosses
633 indicate extreme data outside the 90% CI. The central bars are notched at the mean value of the aggregated
634 data, which represents bias for a specific measurement day or location. Measurement bias (quantified as
635 the mean source rate RER at a particular site or on a particular measurement day) varied moderately on a
636 site-by-site basis, from 0.89 to 0.99, and significantly on a day-to-day basis, from 0.53 to 1.74. This implies
637 that bias on any one day and/or at any one site can be significant; however, available data also imply that,
638 on average, bias across multiple days/sites is not statistically different than unity at a 5% significance level.

639 Figure 4b provides insight into the source of bias variability by showing the same box-whisker diagrams
640 for the RER in modelled 3-m wind speed from Meteoblue (used in Bridger's quantification) vs. the actual
641 measured wind speed. As evidenced by these figures, day-to-day bias errors in estimated source rate

642 correlate with the errors in the modelled 3-m wind speed ($\rho = 0.974$), implying that source rate bias on a
 643 day-to-day basis is driven by error in the windspeed. By contrast, source rate and wind speed bias are
 644 negligibly correlated on a site-by-site basis ($\rho = 0.048$). This implies that, at least for the present dataset,
 645 site-specific sources of bias like surface albedo and site infrastructure that affects wind speed error may be
 646 unimportant relative to day-to-day variability in wind speed error.



647
 648 **Figure 4: Box-whisker diagrams for the relative error ratio (RER) of source rate using Bridger's**
 649 **estimates with Meteoblue wind data, accumulated by measurement day (a) and site (b). The central**
 650 **bars of the box-whisker diagrams are notched at the mean error (i.e., bias) and span the**
 651 **interquartile range; whiskers correspond to the 90% equal tail confidence interval (CI) and red**
 652 **crosses mark extreme data outside the 90% CI. Day-to-day variability is significant with bias**
 653 **errors ranging from 0.53 to 1.74.**

654 Thus, while Eq. (6) is the only practical error model when constrained by limited controlled released data,
 655 Eq. (5) is preferred to avoid underestimation of uncertainties given the potential significance of day-to-day
 656 variability in measurement bias. The difference between these approaches is demonstrated in Figure 3c,
 657 where the present controlled release data for Bridger's GML from four sites over eight unique days in two
 658 different years is sufficient to model uncertainties via either Eq. (5) or (6). Use of Eq. (5) in place of the
 659 simplified Eq. (6) yielded no meaningful effect on the average bias, which changed less than 1.5%.
 660 However, as shown in the figure, and expected given the proper consideration of bias variability, Eq. (5)
 661 estimates higher dispersion in source rate RER (33% increase in standard deviation of RER) than Eq. (6).
 662 This increased variability when considering day- and site-dependent bias is moderate but not insignificant,
 663 and implies an underestimation of quantification uncertainty if controlled release data are limited to a small
 664 number of locations and/or measurement days and Eq. (6) is used for quantification error analysis. Based
 665 on these results, it is highly recommended that future controlled release studies be completed from a range
 666 of unique locations and over as many different days as feasible.

667 **4.3 Limitations**

668 The methodology presented in this manuscript permits derivation of physically realistic and continuous
669 POD functions and robust quantification error models for aerial methane measurement technologies. The
670 application of these new methods to the three example technologies provides informative results for use in
671 other studies but are inherently specific to the data available at the time of publication.

672 Depending on the design of existing controlled release experiments, available data may be insufficient
673 to fully resolve the sensitivities of the POD function and quantification error model to source location (i.e.,
674 terrain and landcover) and measurement date (i.e., weather conditions and optical drift). As identified in
675 Section 4.2.1, site-to-site and day-to-day variability in quantification bias can be significant and future
676 studies should strive to perform experiments at a variety of sites/locations over as many days as feasible to
677 permit construction of error models via Eq. (5). Moreover, Section S3 the SI, which includes a comparison
678 of the optimized POD function for Kairos' LeakSurveyor using only semi- or only non-blinded detections,
679 identifies the need for future third-party studies that focus on rigorous experimental blinding; this is
680 especially needed for the passive imaging spectrometers. Lastly, to maximize the accuracy of any empirical
681 model it is important that controlled release experiments are performed in realistic situations. This includes
682 releases among active oil and gas infrastructure that influence the complex wind field driving plume
683 propagation and may introduce confounding emissions that affect (reduce or enhance) the ability to detect
684 and accurately quantify sources with overlapping plumes.

685 **5 Conclusions**

686 Generalized models to characterize probabilities of detection and quantification error were developed and
687 applied to three aerial methane-detection technologies: Bridger Photonics Inc.'s Gas-Mapping LiDAR
688 (GML), Kairos Aerospace's LeakSurveyor, and the (U.S.) National Aeronautic and Space Administration's
689 Jet Propulsion Laboratory's Next-Generation Airborne Visible/Infrared Imaging Spectrometer (AVIRIS-
690 NG). Leveraging binary regression with a generalized predictor function, this new method improves upon
691 existing techniques in the literature by enabling derivation of continuous and physically realizable POD
692 functions that are variable on methane source rate, ambient wind speed, and aircraft altitude (where
693 available). POD functions optimized to available controlled release data identified technology-specific
694 detection sensitivities that vary with wind speed and altitude. At typical/target aircraft altitudes and a
695 representative average wind speed of 3 m/s, Bridger's GML, Kairos' LeakSurveyor, and AVIRIS-NG were
696 predicted to identify methane emissions of 1.2, 27/32, and 8.1/21 kg/h with 50% probability, respectively,
697 where the latter two lower/upper values depend on whether partial, human-reviewed detections are
698 considered as detections or not).

699 Using a subset of controlled release data for Bridger’s GML and Kairos’ LeakSurveyor that included
700 source rate estimates for comparison with ground truth, controlled source rates, quantification uncertainties
701 were separately characterized, including analysis of effects of using four optional database sources of wind
702 speed for Kairos’ LeakSurveyor. The developed statistical model permits analysis of measurement bias,
703 *variability* in measurement bias (where data permitted), and measurement precision, where the latter two
704 were treated as probabilistic variables. Using the Meteoblue wind speed data product, the source rate
705 relative error ratio (RER – i.e., controlled over estimated source rate) for Bridger’s GML averaged to 0.92
706 with a 95% confidence interval of 0.31-2.13. The analysis of Kairos’ LeakSurveyor identify that source
707 rate RER was highly sensitive to the wind speed data source and statistic (i.e., gust vs. average wind speed)
708 and gust wind speed provided significantly less-biased results. One-minute gust wind speed from the Dark
709 Sky database and one-hour gust wind speed from the HRRR database yielded mean source rate RERs of
710 1.07 and 1.34 with 95% confidence intervals of 0.45-2.17 and 0.57-3.74, respectively. Data from the
711 present controlled release study of Bridger’s GML demonstrated that day-to-day variability in measurement
712 bias was strongly correlated with wind speed error and appreciably increased the dispersion of the source
713 rate RER. These results identify the need to target an assortment of different measurement locations and
714 maximize measurement days during future controlled release studies.

715 Ultimately, the described methods – successfully applied to three example technologies – yield the
716 robustly derived continuous POD function and probabilistic quantification error model that are needed to
717 properly simulate emissions abatement/reduction and support methane monitoring, reporting, and
718 verification via aircraft-based remote sensing. Moreover, the developed generalized methods are readily
719 extensible to analysis of other remote sensing techniques or can be used to update POD and uncertainty
720 models as further controlled release data become publicly available.

721 **Funding**

722 This work was supported by Natural Resources Canada (NRCan, grant number EIP2-MET-001), Natural
723 Sciences and Engineering Research Council of Canada (grant numbers 06632 and 522658), Environment
724 and Climate Change Canada (ECCC, contract number 300071420), and Environmental Defense Fund.

725 **Declaration of Competing Interest**

726 The authors have no competing interests to declare.

727 **Acknowledgements**

728 This project was possible only through the expertise of members of the Energy & Emissions Research Lab
729 who participated in the 2020 and/or 2021 field experiments, including Scott Seymour, Simon Festa-
730 Bianchet, Zachary Milani, Ellen McCole, Cameron Roth, Damon Burt, Parvin Mehr, Milad Mohammadi,
731 and Fraser Kirby with additional support from Brigid Bedard-Hinz, Alex Szekeres, and Reese Bartlett
732 (GreenPath Energy Ltd.). The authors are especially grateful to Mark Anderson (Husky Energy Ltd.) for
733 arranging site access to make the semi- and fully blinded release work possible and to Michael Layer and
734 Nicole MacDonald (Natural Resources Canada), Don D'Souza (British Columbia Ministry of Environment
735 and Climate Change Strategy), and James Diamond (Environment & Climate Change Canada) for their
736 leadership in initiating this and related methane survey work in our lab. Finally, the support of BC Oil and
737 Gas Methane Emissions Research Collaborative (MERC) in parallel work applying these results is
738 gratefully acknowledged.

739 **Supplementary Information**

740 Supplementary information to this article can be found online.

741 **References**

- 742 AER, 2021. Alternative Fugitive Emission Management Program Approvals [WWW Document].
743 URL [https://www.aer.ca/protecting-what-matters/holding-industry-accountable/industry-
performance/methane-performance/alternative-fugitive-emission-management-program-
approvals](https://www.aer.ca/protecting-what-matters/holding-industry-accountable/industry-
744 performance/methane-performance/alternative-fugitive-emission-management-program-
745 approvals) (accessed 2.15.21).
- 746 Apple Inc., 2022. Dark Sky API [WWW Document]. URL <https://darksky.net/dev> (accessed
747 6.9.22).
- 748 Arias, P.A., Bellouin, N., Coppola, E., Jones, R.G., Krinner, G., Marotzke, J., Naik, V., Palmer,
749 M.D., Plattner, G.-K., Rogelj, J., Rojas, M., Sillmann, J., Storelvmo, T., Thorne, P.W.,
750 Trewin, B., Rao, K.A., Adhikary, B., Allan, R.P., Armour, K., Bala, G., Barimalala, R.,
751 Berger, S., Canadell, J.G., Cassou, C., Cherchi, A., Collins, W., Collins, W.D., Connors, S.L.,
752 Corti, S., Cruz, F., Dentener, F.J., Dereczynski, C., Luca, A. Di, Niang, A.D., Doblus-Reyes,
753 F.J., Dosio, A., Douville, H., Engelbrecht, F., Eyring, V., Fischer, E., Forster, P., Fox-
754 Kemper, B., Fuglestedt, J.S., Fyfe, J.C., Gillett, N.P., Goldfarb, L., Gorodetskaya, I.,
755 Gutierrez, J.M., Hamdi, R., Hawkins, E., Hewitt, H.T., Hope, P., Islam, A.S., Jones, C.,
756 Kaufman, D.S., Kopp, R.E., Kosaka, Y., Kossin, J., Krakovska, S., Lee, J.-Y., Li, J.,
757 Mauritsen, T., Maycock, T.K., Meinshausen, M., Min, S.-K., Monteiro, P.M.S., Ngo-Duc, T.,
758 Otto, F., Pinto, I., Pirani, A., Raghavan, K., Ranasinghe, R., Ruane, A.C., Ruiz, L., Sallée, J.-
759 B., Samset, B.H., Sathyendranath, S., Seneviratne, S.I., Sörensson, A.A., Szopa, S.,
760 Takayabu, I., A.-M.Tréguier, Hurk, B. van den, R.Vautard, Schuckmann, K. von, Zaehle, S.,
761 Zhang, X., Zickfeld, K., 2021. Technical Summary, in: Masson-Delmott, V., Zhai, P., Pirani,
762 A., Connors, S.L., Péan, C., Berger, S., Caud, N., Chen, Y., Goldfarb, L., Gomis, M.I., Huang,
763 M., Leitzell, K., Lonnoy, E., Matthews, J.B.R., Maycock, T.K., Waterfield, T., Yelekçi, O.,

764 Yu, R., Zhou, B. (Eds.), *Climate Change 2021: The Physical Science Basis. Contribution of*
765 *Working Group I to the Sixth Assessment Report of the Intergovernmental Panel on Climate*
766 *Change.* Cambridge University Press, pp. 33–144.
767 <https://doi.org/10.1017/9781009157896.002>

768 ARPA-E, 2018. Impact Sheet - Bridger Photonics (MONITOR) [WWW Document]. URL
769 <https://arpa-e.energy.gov/impact-sheet/bridger-photonics-monitor> (accessed 5.23.22).

770 Bell, C., Vaughn, T.L., Zimmerle, D.J., 2020. Evaluation of next generation emission
771 measurement technologies under repeatable test protocols. *Elem Sci Anth* 8, 32.
772 <https://doi.org/10.1525/elementa.426>

773 Berman, E., S.F., W., B., E., Jones, B.B., 2021. Kairos Aerospace Technical White Paper: Methane
774 Detection (Version 1F). Kairos Aerospace. <https://doi.org/10.17605/OSF.IO/HZG52>

775 Branson, K., Jones, B.B., Berman, E.S.F., 2021. Methane Emissions Quantification (No. Version
776 2). Kairos Aerospace, Mountain View, CA.

777 Bridger Photonics, 2022. Gas Mapping LiDAR gains regulatory approval for ALARM use in New
778 Mexico [WWW Document]. URL [https://www.bridgerphotonics.com/blog/gas-mapping-](https://www.bridgerphotonics.com/blog/gas-mapping-lidar-gains-regulatory-approval-alarm-use-new-mexico)
779 [lidar-gains-regulatory-approval-alarm-use-new-mexico](https://www.bridgerphotonics.com/blog/gas-mapping-lidar-gains-regulatory-approval-alarm-use-new-mexico) (accessed 5.23.22).

780 Bridger Photonics, 2021. Gas Mapping LiDAR™ [WWW Document]. URL
781 <https://www.bridgerphotonics.com/gas-mapping-lidar> (accessed 5.31.21).

782 CCAC, 2021. Global Methane Pledge [WWW Document]. URL
783 <https://www.globalmethanepledge.org/> (accessed 4.28.22).

784 Chen, Y., Sherwin, E.D., Berman, E.S.F., Jones, B.B., Gordon, M.P., Wetherley, E.B., Kort, E.A.,
785 Brandt, A.R., 2022. Quantifying Regional Methane Emissions in the New Mexico Permian
786 Basin with a Comprehensive Aerial Survey. *Environ. Sci. Technol.* 56, 4317–4323.
787 <https://doi.org/10.1021/acs.est.1c06458>

788 Cusworth, D.H., Duren, R.M., Thorpe, A.K., Olson-Duvall, W., Heckler, J., Chapman, J.W.,
789 Eastwood, M.L., Helmlinger, M.C., Green, R.O., Asner, G.P., Dennison, P.E., Miller, C.E.,
790 2021. Intermittency of Large Methane Emitters in the Permian Basin. *Environ. Sci. Technol.*
791 *Lett.* 8, 567–573. <https://doi.org/10.1021/acs.estlett.1c00173>

792 Cusworth, D.H., Duren, R.M., Thorpe, A.K., Tseng, E., Thompson, D., Guha, A., Newman, S.,
793 Foster, K.T., Miller, C.E., 2020. Using remote sensing to detect, validate, and quantify
794 methane emissions from California solid waste operations. *Environ. Res. Lett.* 15.
795 <https://doi.org/10.1088/1748-9326/ab7b99>

796 Cusworth, D.H., Jacob, D.J., Varon, D.J., Chan Miller, C., Liu, X., Chance, K., Thorpe, A.K.,
797 Duren, R.M., Miller, C.E., Thompson, D.R., Frankenberg, C., Guanter, L., Randles, C.A.,
798 2019. Potential of next-generation imaging spectrometers to detect and quantify methane
799 point sources from space. *Atmos. Meas. Tech.* 12, 5655–5668. [https://doi.org/10.5194/amt-](https://doi.org/10.5194/amt-12-5655-2019)
800 [12-5655-2019](https://doi.org/10.5194/amt-12-5655-2019)

801 Duren, R.M., Thorpe, A.K., Foster, K.T., Rafiq, T., Hopkins, F.M., Yadav, V., Bue, B.D.,
802 Thompson, D.R., Conley, S., Colombi, N.K., Frankenberg, C., McCubbin, I.B., Eastwood,
803 M.L., Falk, M., Herner, J.D., Croes, B.E., Green, R.O., Miller, C.E., 2019. California's
804 methane super-emitters. *Nature* 575, 180–184. <https://doi.org/10.1038/s41586-019-1720-3>

805 Elder, C.D., Thompson, D.R., Thorpe, A.K., Hanke, P., Walter Anthony, K.M., Miller, C.E., 2020.
806 Airborne Mapping Reveals Emergent Power Law of Arctic Methane Emissions. *Geophys.*
807 *Res. Lett.* 47. <https://doi.org/10.1029/2019GL085707>

808 European Commission, 2021. Proposal for a Regulation of the European Parliament and of the
809 Council on methane emissions reduction in the energy sector and amending Regulation (EU)
810 2019/942. European Commission, Brussels.

811 Foote, M.D., Dennison, P.E., Thorpe, A.K., Thompson, D.R., Jongaramrungruang, S.,
812 Frankenberg, C., Joshi, S.C., 2020. Fast and Accurate Retrieval of Methane Concentration
813 From Imaging Spectrometer Data Using Sparsity Prior. *IEEE Trans. Geosci. Remote Sens.*
814 58, 6480–6492. <https://doi.org/10.1109/TGRS.2020.2976888>

815 Fox, T.A., Barchyn, T.E., Risk, D., Ravikumar, A.P., Hugenholtz, C.H., 2019. A review of close-
816 range and screening technologies for mitigating fugitive methane emissions in upstream oil
817 and gas. *Environ. Res. Lett.* 14, 053002. <https://doi.org/10.1088/1748-9326/ab0cc3>

818 Frankenberg, C., Thorpe, A.K., Thompson, D.R., Hulley, G., Kort, E.A., Vance, N., Borchardt, J.,
819 Krings, T., Gerilowski, K., Sweeney, C., Conley, S.A., Bue, B.D., Aubrey, A.D., Hook, S.,
820 Green, R.O., 2016. Airborne methane remote measurements reveal heavytail flux distribution
821 in Four Corners region. *Proc. Natl. Acad. Sci. U. S. A.* 113, 9734–9739.
822 <https://doi.org/10.1073/pnas.1605617113>

823 Green, R.O., Eastwood, M.L., Sarture, C.M., Chrien, T.G., Aronsson, M., Chippendale, B.J.,
824 Faust, J.A., Pavri, B.E., Chovit, C.J., Solis, M., Olah, M.R., Williams, O., 1998. Imaging
825 Spectroscopy and the Airborne Visible/Infrared Imaging Spectrometer (AVIRIS). *Remote*
826 *Sens. Environ.* 65, 227–248. [https://doi.org/10.1016/S0034-4257\(98\)00064-9](https://doi.org/10.1016/S0034-4257(98)00064-9)

827 Guha, A., Newman, S., Fairley, D., Dinh, T.M., Duca, L., Conley, S.C., Smith, M.L., Thorpe,
828 A.K., Duren, R.M., Cusworth, D.H., Foster, K.T., Fischer, M.L., Jeong, S., Yesiller, N.,
829 Hanson, J.L., Martien, P.T., 2020. Assessment of Regional Methane Emission Inventories
830 through Airborne Quantification in the San Francisco Bay Area. *Environ. Sci. Technol.* 54,
831 9254–9264. <https://doi.org/10.1021/acs.est.0c01212>

832 Hamlin, L., Green, R.O., Mouroulis, P., Eastwood, M., Wilson, D., Dudik, M., Paine, C., 2011.
833 Imaging spectrometer science measurements for Terrestrial Ecology: AVIRIS and new
834 developments, in: 2011 Aerospace Conference. IEEE, pp. 1–7.
835 <https://doi.org/10.1109/AERO.2011.5747395>

836 Hanna, S.R., Briggs, G.A., Hosker Jr., R.P., 1982. Handbook on atmospheric diffusion.

837 Hunter, D., Thorpe, M.J., 2017. Gas Mapping LiDAR Aerial Verification Program Final Report.
838 Alberta Upstream Petroleum Research Fund Project 17-ARPC-03, Petroleum Technology
839 Alliance of Canada (PTAC).

840 InvestableUniverse, 2021. Breakthrough For LiDAR Tech In Oil And Gas Industry After Exxon
841 Filing [WWW Document]. URL [https://investableuniverse.com/2021/04/09/bridger-
842 photonics-lidar-methane-emissions-exxon-mobil/](https://investableuniverse.com/2021/04/09/bridger-photonics-lidar-methane-emissions-exxon-mobil/) (accessed 5.23.22).

843 IPCC, 2018. Summary for Policymakers, in: Masson-Delmotte, V., Zhai, P., Pörtner, H.-O.,
844 Roberts, D., Skea, J., Shukla, P.R., Pirani, A., Moufouma-Okia, W., Péan, C., Pidcock, R.,
845 Connors, S., Matthews, J.B.R., Chen, Y., Zhou, X., Gomis, M.I., Lonnoy, E., Maycock, T.,
846 Tignor, M., Waterfield, T. (Eds.), *Global Warming of 1.5°C. An IPCC Special Report on the*
847 *Impacts of Global Warming of 1.5°C above Pre-Industrial Levels. Intergovernmental Panel*
848 *on Climate Change.*

849 Jervis, D., McKeever, J., Durak, B.O.A., Sloan, J.J., Gains, D., Varon, D.J., Ramier, A., Strupler,
850 M., Tarrant, E., 2021. The GHGSat-D imaging spectrometer. *Atmos. Meas. Tech.* 14, 2127–
851 2140. <https://doi.org/10.5194/amt-14-2127-2021>

852 Johnson, M.R., Tyner, D.R., Szekeres, A.J., 2021. Blinded evaluation of airborne methane source
853 detection using Bridger Photonics LiDAR. *Remote Sens. Environ.* 259, 112418.
854 <https://doi.org/10.1016/j.rse.2021.112418>

855 Kairos Aerospace, 2022a. New Mexico Authority Approves Kairos Aerospace Technology in
856 Methane Emissions Mitigation Efforts [WWW Document]. URL
857 [https://kairosaerospace.com/new-mexico-authority-approves-kairos-aerospace-technology-](https://kairosaerospace.com/new-mexico-authority-approves-kairos-aerospace-technology-in-methane-emissions-mitigation-efforts/)
858 [in-methane-emissions-mitigation-efforts/](https://kairosaerospace.com/new-mexico-authority-approves-kairos-aerospace-technology-in-methane-emissions-mitigation-efforts/) (accessed 6.2.22).

859 Kairos Aerospace, 2022b. Methane Detection from a Unique Perspective [WWW Document].
860 URL <https://kairosaerospace.com/methane-detection/> (accessed 5.29.22).

861 Kass, R.E., Raftery, A.E., 1995. Bayes Factors. *J. Am. Stat. Assoc.* 90, 773–795.

862 Kemp, C.E., Ravikumar, A.P., 2021. New Technologies Can Cost Effectively Reduce Oil and Gas
863 Methane Emissions, but Policies Will Require Careful Design to Establish Mitigation
864 Equivalence. *Environ. Sci. Technol.* 55, 9140–9149. <https://doi.org/10.1021/acs.est.1c03071>

865 Kemp, C.E., Ravikumar, A.P., Brandt, A.R., 2016. Comparing Natural Gas Leakage Detection
866 Technologies Using an Open-Source “virtual Gas Field” Simulator. *Environ. Sci. Technol.*
867 50, 4546–4553. <https://doi.org/10.1021/acs.est.5b06068>

868 Krautwurst, S., Gerilowski, K., Jonsson, H.H., Thompson, D.R., Kolyer, R.W., Iraci, L.T., Thorpe,
869 A.K., Horstjann, M., Eastwood, M., Leifer, I., Vigil, S.A., Krings, T., Borchardt, J., Buchwitz,
870 M., Fladeland, M.M., Burrows, J.P., Bovensmann, H., 2017. Methane emissions from a
871 Californian landfill, determined from airborne remote sensing and in situ measurements.
872 *Atmos. Meas. Tech.* 10, 3429–3452. <https://doi.org/10.5194/amt-10-3429-2017>

873 Kreitinger, A.T., Thorpe, M.J., 2018. High-Sensitivity Gas-Mapping 3D Imager and Method of
874 Operation. 9970756 B2.

875 NOAA, 2020. High-Resolution Rapid Refresh (HRRR) Model [WWW Document]. URL
876 <https://rapidrefresh.noaa.gov/> (accessed 6.9.22).

877 Rashid, K., Speck, A., Osedach, T.P., Perroni, D. V., Pomerantz, A.E., 2020. Optimized inspection
878 of upstream oil and gas methane emissions using airborne LiDAR surveillance. *Appl. Energy*
879 275, 115327. <https://doi.org/10.1016/j.apenergy.2020.115327>

880 Ravikumar, A.P., Sreedhara, S., Wang, J., Englander, J.G., Roda-Stuart, D., Bell, C.S., Zimmerle,
881 D.J., Lyon, D.R., Mogstad, I., Ratner, B., Brandt, A.R., 2019. Single-blind inter-comparison
882 of methane detection technologies – results from the Stanford/EDF Mobile Monitoring
883 Challenge. *Elem Sci Anth* 7, 37. <https://doi.org/10.1525/elementa.373>

884 Schwietzke, S., Harrison, M., Lauderdale, T., Branson, K., Conley, S.A., George, F.C., Jordan, D.,
885 Jersey, G.R., Zhang, C., Mairs, H.L., Pétron, G., Schnell, R.C., 2019. Aerially guided leak
886 detection and repair: A pilot field study for evaluating the potential of methane emission
887 detection and cost-effectiveness. *J. Air Waste Manag. Assoc.* 69, 71–88.
888 <https://doi.org/10.1080/10962247.2018.1515123>

889 Sherwin, E.D., Chen, Y., Ravikumar, A.P., Brandt, A.R., 2021. Single-blind test of airplane-based
890 hyperspectral methane detection via controlled releases. *Elem. Sci. Anthr.* 9.
891 <https://doi.org/10.1525/elementa.2021.00063>

892 Snipes, M., Taylor, D.C., 2014. Model selection and Akaike Information Criteria: An example
893 from wine ratings and prices. *Wine Econ. Policy* 3, 3–9.
894 <https://doi.org/10.1016/j.wep.2014.03.001>

- 895 Thompson, D.R., Leifer, I., Bovensmann, H., Eastwood, M., Fladeland, M., Frankenberg, C.,
896 Gerilowski, K., Green, R.O., Kratwurst, S., Krings, T., Luna, B., Thorpe, A.K., 2015. Real-
897 time remote detection and measurement for airborne imaging spectroscopy: a case study with
898 methane. *Atmos. Meas. Tech.* 8, 4383–4397. <https://doi.org/10.5194/amt-8-4383-2015>
- 899 Thorpe, A.K., Duren, R.M., Conley, S., Prasad, K.R., Bue, B.D., Yadav, V., Foster, K.T., Rafiq,
900 T., Hopkins, F.M., Smith, M.L., Fischer, M.L., Thompson, D.R., Frankenberg, C.,
901 McCubbin, I.B., Eastwood, M.L., Green, R.O., Miller, C.E., 2020. Methane emissions from
902 underground gas storage in California. *Environ. Res. Lett.* 15, 045005.
903 <https://doi.org/10.1088/1748-9326/ab751d>
- 904 Thorpe, A.K., Frankenberg, C., Aubrey, A.D., Roberts, D.A., Nottrott, A.A., Rahn, T.A., Sauer,
905 J.A., Dubey, M.K., Costigan, K.R., Arata, C., Steffke, A.M., Hills, S., Haselwimmer, C.,
906 Charlesworth, D., Funk, C.C., Green, R.O., Lundeen, S.R., Boardman, J.W., Eastwood, M.L.,
907 Sarture, C.M., Nolte, S.H., Mccubbin, I.B., Thompson, D.R., McFadden, J.P., 2016. Mapping
908 methane concentrations from a controlled release experiment using the next generation
909 airborne visible/infrared imaging spectrometer (AVIRIS-NG). *Remote Sens. Environ.* 179,
910 104–115. <https://doi.org/10.1016/j.rse.2016.03.032>
- 911 Thorpe, A.K., Frankenberg, C., Thompson, D.R., Duren, R.M., Aubrey, A.D., Bue, B.D., Green,
912 R.O., Gerilowski, K., Krings, T., Borchardt, J., Kort, E.A., Sweeney, C., Conley, S., Roberts,
913 D.A., Dennison, P.E., 2017. Airborne DOAS retrievals of methane, carbon dioxide, and water
914 vapor concentrations at high spatial resolution: Application to AVIRIS-NG. *Atmos. Meas.*
915 *Tech.* 10, 3833–3850. <https://doi.org/10.5194/amt-10-3833-2017>
- 916 Thorpe, A.K., O’Handley, C., Emmitt, G.D., DeCola, P.L., Hopkins, F.M., Yadav, V., Guha, A.,
917 Newman, S., Herner, J.D., Falk, M., Duren, R.M., 2021. Improved methane emission
918 estimates using AVIRIS-NG and an Airborne Doppler Wind Lidar. *Remote Sens. Environ.*
919 266, 112681. <https://doi.org/10.1016/j.rse.2021.112681>
- 920 Tyner, D.R., Johnson, M.R., 2021. Where the Methane Is—Insights from Novel Airborne LiDAR
921 Measurements Combined with Ground Survey Data. *Environ. Sci. Technol.* 55, 9773–9783.
922 <https://doi.org/10.1021/acs.est.1c01572>
- 923 Varon, D.J., Jacob, D.J., Jervis, D., McKeever, J., 2020. Quantifying Time-Averaged Methane
924 Emissions from Individual Coal Mine Vents with GHGSat-D Satellite Observations. *Environ.*
925 *Sci. Technol.* 54, 10246–10253. <https://doi.org/10.1021/acs.est.0c01213>
- 926 Varon, D.J., Jacob, D.J., McKeever, J., Jervis, D., Durak, B.O.A., Xia, Y., Huang, Y., 2018.
927 Quantifying methane point sources from fine-scale satellite observations of atmospheric
928 methane plumes. *Atmos. Meas. Tech.* 11, 5673–5686. <https://doi.org/10.5194/amt-11-5673-2018>

930 List of Figure Captions

931 **Figure 1: Available controlled release data for (a,b) Bridger Photonics GML, (c,d) Kairos LeakSurveyor, and**
932 **(e,f) AVIRIS-NG. Successful detections are outlined in blue (fully blinded data), green (semi-blinded data),**
933 **or black (non-blinded data); partial detections in purple; and missed detections in red. Righthand panels (b,**
934 **d, and f) show a zoomed subset of lower release rate data from the corresponding left panels, where the data**
935 **points are also shaded according to each technique’s simple predictor function (described in the main text) as**
936 **outlined on the right of each panel.**

937 **Figure 2: Robustly derived probability of detection (POD) functions for Bridger’s GML technology, Kairos’**
938 **LeakSurveyor technology, and AVIRIS-NG. a-c) detection success against optimized predictor function**
939 **values for all available controlled release data for each instrument alongside the corresponding optimized**
940 **inverse link function (green line). d-f) calculated probability of detection as a function of source rate and 3-m**
941 **wind speed at typical flight altitudes (corresponding approximate swath widths also shown) for each**
942 **instrument. Contours for probabilities of detection of 10, 50, and 90% and their associated functions (Q_p) are**
943 **overlaid in each plot as solid lines. For comparison, POD contours if partial detections are included are also**
944 **plotted with their associated functions (Q'_p) as dashed lines. Table 2 provides general equations for POD as a**
945 **function of source rate, wind speed, and altitude (where relevant) for all cases in this figure.**

946 **Figure 3: Summary of controlled release data and quantification error analysis for a) Bridger’s GML**
947 **technology using Meteoblue wind data (purple) and b) Kairos’ LeakSurveyor technology, computed using**
948 **Dark Sky one-minute average (green) and gust (yellow) and HRRR hourly average (red) and gust (blue) wind**
949 **data. (c) Resulting distributions of the source rate relative error ratio (RER) for each technique and wind**
950 **source via fitting of Eq. (6) in addition to the source rate RER for Bridger’s GML technology using Eq. (5).**
951 **Distribution means, representing quantification bias error are identified for each distribution by a point.**

952 **Figure 4: Box-whisker diagrams for the relative error ratio (RER) of source rate using Bridger’s estimates**
953 **with Meteoblue wind data, accumulated by measurement day (a) and site (b). The central bars of the box-**
954 **whisker diagrams are notched at the mean error (i.e., bias) and span the interquartile range; whiskers**
955 **correspond to the 90% equal tail confidence interval (CI) and red crosses mark extreme data outside the 90%**
956 **CI. Day-to-day variability is significant with bias errors ranging from 0.53 to 1.74.**

1 **Supplemental Information**

2
3 **Robust Probabilities of Detection and Quantification Uncertainty**
4 **for Aerial Methane Detection: Examples for Three Airborne**
5 **Technologies**

6 **Bradley M. Conrad, David R. Tyner, Matthew R. Johnson***

7 *Energy & Emissions Research Laboratory,*
8 *Department of Mechanical and Aerospace Engineering,*
9 *Carleton University, Ottawa, ON, Canada, K1S 5B6*

10
11 *Corresponding author: Matthew.Johnson@carleton.ca

12 **S1 Facilities for High-Flowrate Controlled Release Experiments of Bridger**
13 **Photonics Inc.'s Gas-Mapping LiDAR**

14 High-flowrate, controlled release experiments were completed to support the present analysis of
15 quantification error for Bridger Photonic Inc.'s Gas-Mapping LiDAR (GML) technology.
16 Expanding on the description in the main text, these were performed at four inactive oil and gas
17 facilities (approximate GPS coordinates: 53.12°N, 109.65°W) located in Western Saskatchewan,
18 Canada and shown in Figure S1. These previously oil-producing facilities were approximately
19 30 km southeast of the town of Lloydminster and each less than 100 m in size in the north-south
20 direction such that they were easily captured in a single swath of Bridger's GML, mounted on an
21 aircraft flying approximately west/eastward. The facilities were sufficiently spaced
22 (approximately 350, 390, and 410 m apart from west to east) to avoid any significant overlap of
23 controlled release plumes granting Bridger the opportunity to measure four controlled releases in
24 quick succession (<30 s at typical flight speeds). The aircraft looped over the facilities
25 approximately every 4 minutes, permitting the ground teams to adjust controlled release rate (semi-
26 blindly) between passes and ensuring detectable plumes from the previous pass were sufficiently
27 dispersed and the new plumes had time to establish.



28
29
30
31
32
33
34
Figure S1: Four inactive, previously oil-producing, facilities used for high-flowrate controlled releases to study Bridger Photonics Inc.'s Gas-Mapping LiDAR technology. The four facilities were approximately 375 m apart in the west-east direction and less than 100 m in size in the north-south direction, permitting measurement of four controlled releases in rapid succession.

35 S2 Model Optimization and Selection

36 This section describes the model optimization and selection procedure for the derived probability
37 of detection (POD) functions ($POD(\mathbf{x})$) and quantification error distributions ($\pi(Q|\tilde{Q})$).

38 The methodology to derive POD functions for a given measurement technology combines a
39 predictor function ($g(\mathbf{x}; \boldsymbol{\phi})$), which is variable on measured parameters and conditions (\mathbf{x}) and
40 parameterized by $\boldsymbol{\phi}$, and an inverse link function ($F(g; \boldsymbol{\theta})$), which is variable on the predictor
41 function output and is parameterized by $\boldsymbol{\theta}$. As discussed in the manuscript, a generalized predictor
42 function of seven optional coefficients was used (Eq. (7) in the manuscript and repeated below for
43 convenience) and candidate inverse link functions included cumulative distribution functions
44 (CDFs) of probability distributions with non-negative support. To avoid over-determination of
45 this optimization problem, the coefficients of the candidate inverse link functions ($\boldsymbol{\theta}$) were
46 constrained such that the distribution represented by the candidate CDF had a unit mean and unit
47 variance. Eight two-parameter probability distributions were considered for the inverse link
48 function including the Fréchet, Gamma, and Loglogistic distributions. The candidate model that
49 minimizes the corrected Akaike Information Criterion (AICc; Akaike, 1974) was deemed optimal.

$$g(\mathbf{x}; \boldsymbol{\phi}) = \phi_7 \frac{(Q_{[\text{kg/h}]} - \phi_1)^{\phi_3}}{\tilde{n}_{[\text{ppm}\cdot\text{m}]}^{\phi_4} \left(\frac{h_{[\text{m}]}}{1000}\right)^{\phi_5} (u_{3[\text{m/s}]} - \phi_2)^{\phi_6}} \quad (7)$$

50 Referring to the predictor function (Eq. (7)) and discussion in the manuscript, coefficients
51 could be optionally fixed to ignore the effect of, for example, scene noise or aircraft altitude on

52 detection probability. With the present controlled release data for Bridger’s GML, for which a
 53 subset included scene noise data, the importance of each coefficient was studied. Firstly, a nominal
 54 *initial* model that minimized the negative log-likelihood (see Eq. (3) in the manuscript) was
 55 obtained. Then, the relative importance of scene noise and aircraft altitude was assessed by
 56 optionally fixing ϕ_4 and/or ϕ_5 to zero and optimizing the POD for the subset of Bridger GML data
 57 where scene noise was available ($N = 178$). The marginal benefit of including an additional non-
 58 fixed coefficient (i.e., ϕ_4 and/or ϕ_5) was assessed using the AICc. This parameter, technically a
 59 “Bayes Factor” (e.g., Snipes and Taylor, 2014), is used to quantify the relative goodness of models
 60 and is a function of the optimized value of the negative log-likelihood function (i.e., the objective
 61 function of the optimization) and with a penalty on number of optimized variables. The difference
 62 in the AICc (ΔAICc) between an *initial model* and an *alternative model* is indicative of the
 63 statistical justification for the latter over the former. This result is typically interpreted using Kass
 64 and Raftery’s (1995) classification, where ΔAICc in $(0, 10^{0.5})$ implies that the difference between
 65 models is “not worth more than a bare mention” and ΔAICc in $(10^{0.5}, 10^1)$ and $(10^1, 10^2)$ imply
 66 that there is “substantial” and “strong” justification for the alternative model over the initial model.
 67 As summarized in Table S1 and discussed in the manuscript, the consideration of scene noise *or*
 68 aircraft altitude is strongly justified ($\Delta\text{AICc} \approx 10^{1.2}$). By contrast, the marginal benefit of including
 69 noise or aircraft altitude if the other is already in the initial model is much weaker, cussing the
 70 “not worth more than a bare mention” classification.

71 **Table S1: Summary of goodness-of-fit statistics for models that incrementally include consideration of**
 72 **representative scene noise or aircraft altitude.**

Initial Model:		Alternative Model:		ΔAICc over Candidate Models
Noise	Altitude	Noise	Altitude	
No	No	No	Yes	$10^{1.20}$
No	No	Yes	No	$10^{1.18}$
No	Yes	Yes	Yes	$10^{0.42}$
Yes	No	Yes	Yes	$10^{0.55}$

73

74 Coefficients (ϕ) of the optimized predictor function ($g(\mathbf{x}; \phi)$) were computed for each
 75 technology: Bridger Photonics Inc.’s Gas-Mapping LiDAR (GML), Kairos Aerospace’s
 76 LeakSurveyor, and AVIRIS-NG (Next-Generation Airborne Visible/Infrared Imaging
 77 Spectrometer) from the (U.S.) National Aeronautics and Space Administration’s (NASA’s) Jet

78 Propulsion Laboratory (JPL). Table S2 provides the complete equations for these predictor
79 functions as well as the inverse link functions ($F(g; \boldsymbol{\theta})$); the composition of these equations yields
80 the POD function ($POD(\boldsymbol{x})$) for each technique, which are detailed in the final column of the
81 table.

82 The quantification error distributions were modeled via Eq. (5) or (6) in the manuscript
83 depending on the assumed (in)dependence of measurement bias with measurement date and
84 location. Regardless of the assumption, quantification error distributions were obtained via MLE
85 using the same eight two-parameter probability distributions used for the optimization of the POD.
86 Likewise, the optimized models were evaluated using the AICc. Table S3 summarizes the results
87 for the quantification error analysis of Bridger's GML and Kairos' LeakSurveyor. The optimized
88 bias-correction functions ($\hat{Q} = f_B(\tilde{Q})$) and bias- and precision-distributions (π_{κ_Q} and π_{λ_Q} as
89 needed, where $\kappa_Q = Q/\tilde{Q}$ and $\lambda_Q = Q/\hat{Q}$) are shown for each of the technologies and wind data
90 sources discussed in the manuscript. These results are combined in the last column of the table to
91 yield the conditional distribution for quantification error, $\pi(Q|\tilde{Q})$. Table S4 summarizes the same
92 analysis for wind speed error distributions, $\pi(u_3|\tilde{u}_3)$ to support calculations via Eq. (10) in the
93 main text. Histograms of the source data and resulting fits for the results presented in Table S3
94 and Table S4 are shown in Figure S2 and Figure S3, respectively.

Table S2: Detailed equations for the predictor, inverse link, and composite POD functions for each measurement technology.

Instrument	Predictor Function $g(Q, u_3, \tilde{h})$	Inverse Link Function $F(g)$	Detailed Equation for POD(Q, u_3, \tilde{h})
Bridger Photonics Inc. GML	$\frac{0.152 Q_{[\text{kg/h}]}^{1.07}}{\left(\frac{\tilde{h}_{[\text{m}]}}{1000}\right)^{2.44} (u_{3[\text{m/s}]} + 2.14)^{1.69}}$	Fréchet CDF: $\exp(-0.372g^{-2.53})$	$\exp\left(-\left(\frac{0.224 Q_{[\text{kg/h}]}^{1.07}}{\left(\frac{\tilde{h}_{[\text{m}]}}{1000}\right)^{2.44} (u_{3[\text{m/s}]} + 2.14)^{1.69}}\right)^{-2.53}\right)$
Kairos Aerospace LeakSurveyor ^a (Excluding Partial Detections)	$\frac{(8.50 \times 10^{-3}) Q_{[\text{kg/h}]}^{1.99}}{(u_{3[\text{m/s}]} + 0.534)^{1.92}}$	Burr CDF: $1 - (1 + g^2)^{-1.5}$	$1 - \left(1 + \left(\frac{(8.50 \times 10^{-3}) Q_{[\text{kg/h}]}^{1.99}}{(u_{3[\text{m/s}]} + 0.534)^{1.92}}\right)^2\right)^{-1.5}$
Kairos Aerospace LeakSurveyor ^a (Including Partial Detections)	$\frac{(7.71 \times 10^{-3}) Q_{[\text{kg/h}]}^{1.87}}{(u_{3[\text{m/s}]})^{1.41}}$	Burr CDF: $1 - (1 + g^2)^{-1.5}$	$1 - \left(1 + \left(\frac{(7.71 \times 10^{-3}) Q_{[\text{kg/h}]}^{1.87}}{(u_{3[\text{m/s}]})^{1.41}}\right)^2\right)^{-1.5}$
AVIRIS-NG (Excluding Partial Detections)	$\frac{(31.1 \times 10^{-3}) Q_{[\text{kg/h}]}^{1.99}}{\left(\frac{\tilde{h}_{[\text{m}]}}{1000}\right)^{1.91} \exp(0.239 u_{3[\text{m/s}]})}$	Burr CDF: $1 - (1 + g^2)^{-1.5}$	$1 - \left(1 + \left(\frac{(31.1 \times 10^{-3}) Q_{[\text{kg/h}]}^{1.99}}{\left(\frac{\tilde{h}_{[\text{m}]}}{1000}\right)^{1.91} \exp(0.239 u_{3[\text{m/s}]})}\right)^2\right)^{-1.5}$
AVIRIS-NG (Including Partial Detections)	$\frac{0.247 Q_{[\text{kg/h}]}^{1.10}}{\left(\frac{\tilde{h}_{[\text{m}]}}{1000}\right)^{0.731} \exp(0.114 u_{3[\text{m/s}]})}$	Fréchet CDF: $\exp(-0.372g^{-2.53})$	$\exp\left(-\left(\frac{0.365 Q_{[\text{kg/h}]}^{1.10}}{\left(\frac{\tilde{h}_{[\text{m}]}}{1000}\right)^{0.731} \exp(0.114 u_{3[\text{m/s}]})}\right)^{-2.53}\right)$

^a Result for Kairos' LeakSurveyor technology at fixed aircraft altitude of 900 m.

Table S3: Optimized bias-correction functions and precision distributions for estimated source rate using Bridger’s GML and Kairos’ LeakSurveyor technologies with various wind speed data. Optimized bias-correction functions were proportional models and precision-correction distributions took the form of various non-negative probability distributions with unit mean. Detailed equations for the resulting quantification error distribution ($\pi(Q|\bar{Q})$) are also provided.

Instrument	Wind Source	Bias-correction Function $f_B(\bar{Q}) = d\bar{Q}$	Bias- and Precision-Correction Distributions ^a π_{κ_Q} and π_{λ_Q}	Detailed Equation for $\pi(Q \bar{Q})$
Bridger Photonics Inc. GML	Meteoblue – Proprietary averaging	$d = 0.918$	$\lambda_Q \sim LL\left(\frac{0.891}{\alpha}, \frac{3.82}{\beta}\right)$	$\frac{\left(\frac{\beta}{\alpha}\right)\left(\frac{Q}{d\alpha\bar{Q}}\right)^{\beta-1}}{d\bar{Q}\left(1 + \left(\frac{Q}{d\alpha\bar{Q}}\right)^\beta\right)^2}$
Bridger Photonics Inc. GML ^b	Meteoblue – Proprietary averaging	$d = 0.932$	$\kappa_Q \sim LL\left(\frac{0.934}{\alpha}, \frac{4.96}{\beta}\right)$ $\lambda_Q \sim LL\left(\frac{0.888}{\alpha}, \frac{3.77}{\beta}\right)$	$\pi(Q \bar{Q}) = \int_{\bar{Q}} \pi_{\lambda_Q}\left(\frac{Q}{\bar{Q}}\right) \pi_{\kappa_Q}\left(\frac{\bar{Q}}{f_B(\bar{Q})}\right) \frac{1}{\bar{Q}f_B(\bar{Q})} d\bar{Q}$
Kairos Aerospace LeakSurveyor	Dark Sky – 1-minute average	$d = 2.14$	$\lambda_Q \sim LL\left(\frac{0.932}{\alpha}, \frac{4.87}{\beta}\right)$	$\frac{\left(\frac{\beta}{\alpha}\right)\left(\frac{Q}{d\alpha\bar{Q}}\right)^{\beta-1}}{d\bar{Q}\left(1 + \left(\frac{Q}{d\alpha\bar{Q}}\right)^\beta\right)^2}$
	Dark Sky – 1-minute gust ^c	$d = 1.07$	$\lambda_Q \sim LN\left(\frac{-0.0808}{\mu}, \frac{0.402}{\sigma}\right)$	$\frac{1}{Q\sigma\sqrt{2\pi}} \exp\left(-\frac{\left(\ln\left(\frac{Q}{d\bar{Q}}\right) - \mu\right)^2}{2\sigma^2}\right)$
	HRRR – 1-hour average	$d = 2.53$	$\lambda_Q \sim Fre\left(\frac{2.04}{\alpha}, \frac{0.575}{s}\right)$	$\frac{\alpha}{sd\bar{Q}} \left(\frac{Q}{sd\bar{Q}}\right)^{-\alpha-1} \exp\left(-\left(\frac{Q}{sd\bar{Q}}\right)^{-\alpha}\right)$
	HRRR – 1-hour gust	$d = 1.34$	$\lambda_Q \sim Fre\left(\frac{2.64}{\alpha}, \frac{0.693}{s}\right)$	

^a Legend: *Fre* = Fréchet distribution; *LL* = Log-logistic distribution; *LN* = Log-normal distribution.

^b Quantification error distribution fit to Bridger GML data assuming time- and location-dependent measurement bias (i.e., fit using Eq. (5) in the manuscript).

^c Includes an additional 296 data from controlled release studies completed by Kairos.

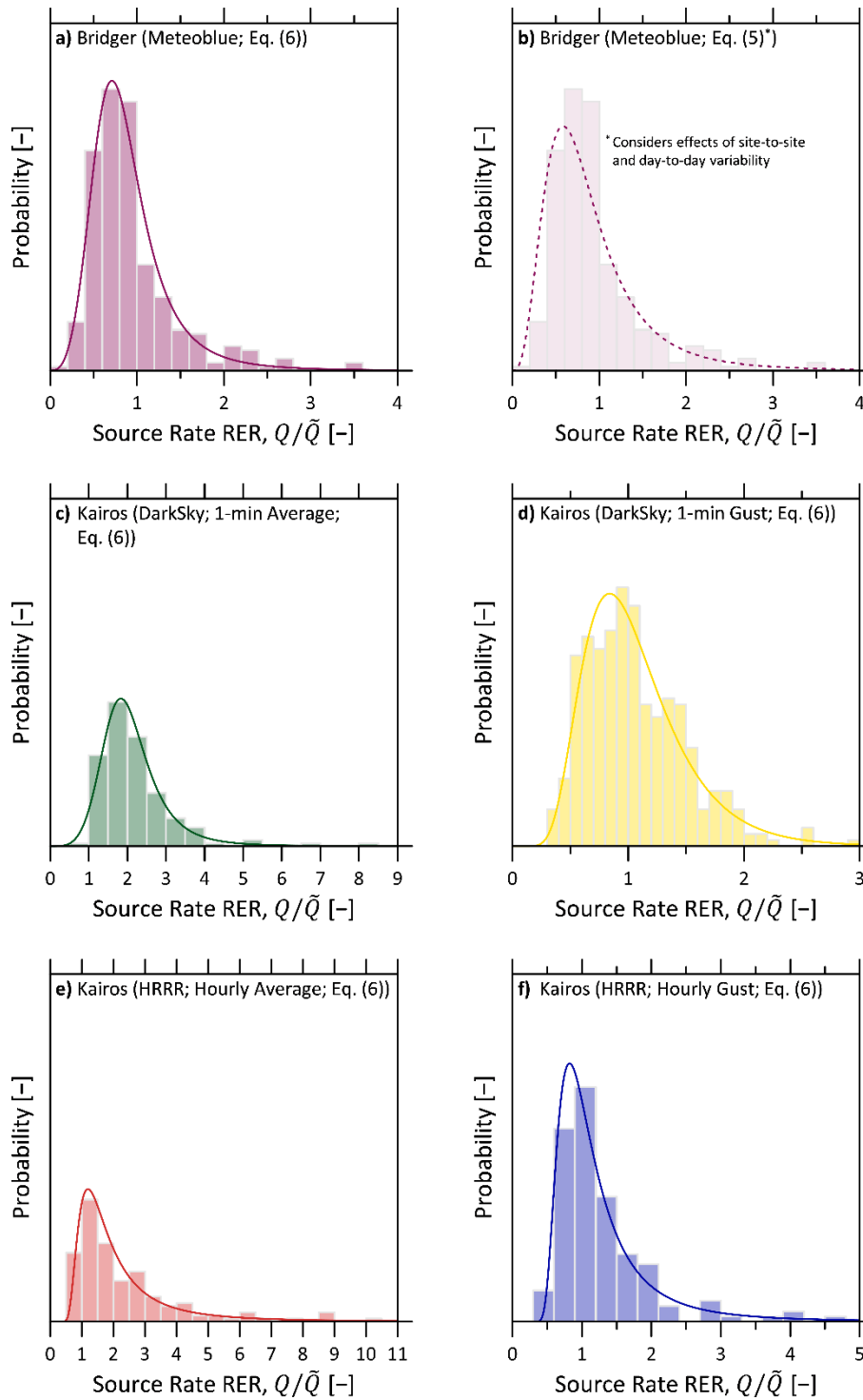
103
104
105
106
107

Table S4: Optimized bias-correction functions and precision distributions for various 3-m wind speed data sources relevant to Bridger’s GML and Kairos’ LeakSurveyor technologies. Optimized bias-correction functions were proportional models and precision-correction distributions took the form of various non-negative probability distributions with unit mean. The detailed equations for the resulting quantification error distribution ($\pi(u_3|\tilde{u}_3)$) are provided for use with Eq. (10) in the main text if seeking to derive POD functions that use modelled wind rather than in situ measured/actual wind.

Instrument	Wind Source	Bias-correction Function $f_B(\tilde{u}_3) = d\tilde{u}_3$	Bias- and Precision-Correction Distributions ^a $\pi_{\kappa_{u_3}}$ and $\pi_{\lambda_{u_3}}$	Detailed Equation for $\pi(u_3 \tilde{u}_3)$
Bridger Photonics Inc. GML	Meteoblue – Proprietary averaging	$d = 0.903$	$\lambda_{u_3} \sim LL\left(\frac{0.903}{\alpha}, \frac{4.05}{\beta}\right)$	$\frac{\left(\frac{\beta}{\alpha}\right)\left(\frac{u_3}{d\alpha\tilde{u}_3}\right)^{\beta-1}}{d\tilde{u}_3\left(1 + \left(\frac{u_3}{d\alpha\tilde{u}_3}\right)^\beta\right)^2}$
Bridger Photonics Inc. GML ^b	Meteoblue – Proprietary averaging	$d = 1.02$	$\kappa_{u_3} \sim Burr\left(\frac{3.47}{c}, \frac{1.29}{k}\right)$ $\lambda_{u_3} \sim Burr\left(\frac{3.36}{c}, \frac{1.30}{k}\right)$	$\pi(u \tilde{u}_3) = \int_{\tilde{u}_3} \pi_{\lambda_{u_3}}\left(\frac{u_3}{\hat{u}_3}\right) \pi_{\kappa_{u_3}}\left(\frac{\hat{u}_3}{f_B(\tilde{u}_3)}\right) \frac{1}{\hat{u}_3 f_B(\tilde{u}_3)} d\hat{u}_3$
Kairos Aerospace LeakSurveyor	Dark Sky – 1-minute average	$d = 1.82$	$\lambda_{u_3} \sim Burr\left(\frac{5.46}{c}, \frac{1.18}{k}\right)$	$\frac{ck}{d\tilde{u}_3} \frac{\left(\frac{u_3}{d\tilde{u}_3}\right)^{c-1}}{\left(1 + \left(\frac{u_3}{d\tilde{u}_3}\right)^c\right)^{k+1}}$
	Dark Sky – 1-minute gust ^c	$d = 0.780$	$\lambda_{u_3} \sim W\left(\frac{1.11}{\xi}, \frac{3.61}{k}\right)$	$\frac{k}{d\xi\tilde{u}_3} \left(\frac{u_3}{d\xi\tilde{u}_3}\right)^{k-1} \exp\left(-\left(\frac{u_3}{d\xi\tilde{u}_3}\right)^k\right)$
	HRRR – 1-hour average	$d = 1.93$	$\lambda_{u_3} \sim IG\left(\frac{1}{\mu}, \frac{2.80}{\xi}\right)$	$\frac{1}{d\tilde{u}_3} \sqrt{\frac{\xi}{2\pi}} \left(\frac{u_3}{d\tilde{u}_3}\right)^{-3} \exp\left(-\frac{d\xi\tilde{u}_3\left(\frac{u_3}{d\tilde{u}_3} - 1\right)^2}{2u_3}\right)$
	HRRR – 1-hour gust	$d = 1.06$	$\lambda_{u_3} \sim LL\left(\frac{0.908}{\alpha}, \frac{4.17}{\beta}\right)$	$\frac{\left(\frac{\beta}{\alpha}\right)\left(\frac{u_3}{d\alpha\tilde{u}_3}\right)^{\beta-1}}{d\tilde{u}_3\left(1 + \left(\frac{u_3}{d\alpha\tilde{u}_3}\right)^\beta\right)^2}$

^a Legend: *Burr* = Burr Type XII (two-parameter) distribution; *IG* = Inverse Gaussian distribution; *LL* = Log-logistic distribution; *W* = Weibull distribution.
^b Quantification error distribution fit to Bridger GML data assuming time- and location-dependent measurement bias (i.e., fit using Eq. (5) in the manuscript).
^c Includes an additional 296 data from controlled release studies completed by Kairos.

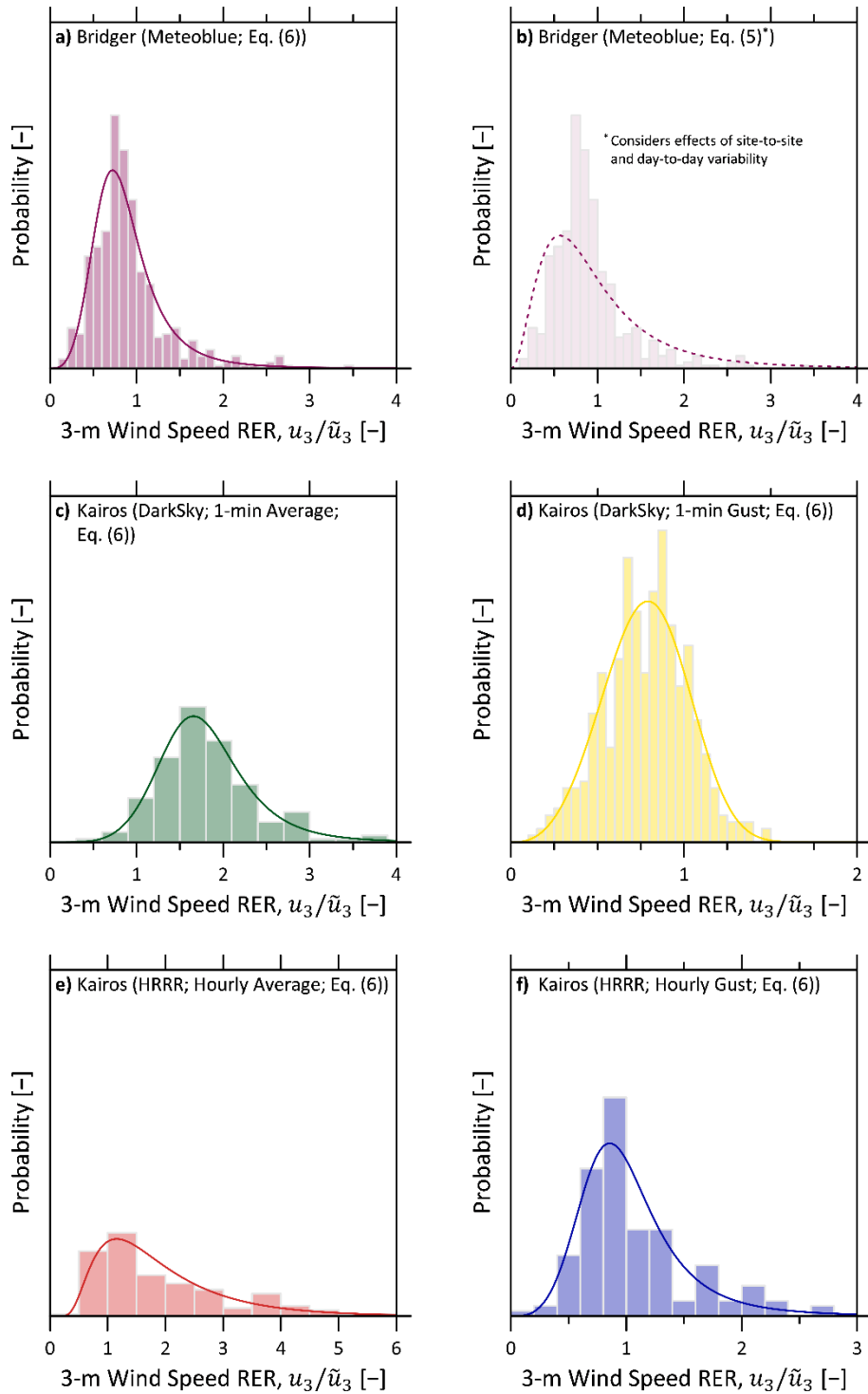
108



109

110 **Figure S2: Histogram and fitted distribution for the source rate relative error ratio (RER).** (a)-(b) Bridger's
 111 GML technology using MeteoBlue wind data as computed via Eq. (6) and (5) in the manuscript, respectively;
 112 The histogram in subplot (b) is shaded and the distribution is dashed to contrast it with the other plots, since
 113 the use of Eq. (5) in this case specifically considers day-to-day and site-to-site variability when determining
 114 the overall bias and precision; (c)-(f) Kairos' LeakSurveyor Technology using four different sources of wind
 115 speed data computed via Eq. (6).

116



117

118

119

120

121

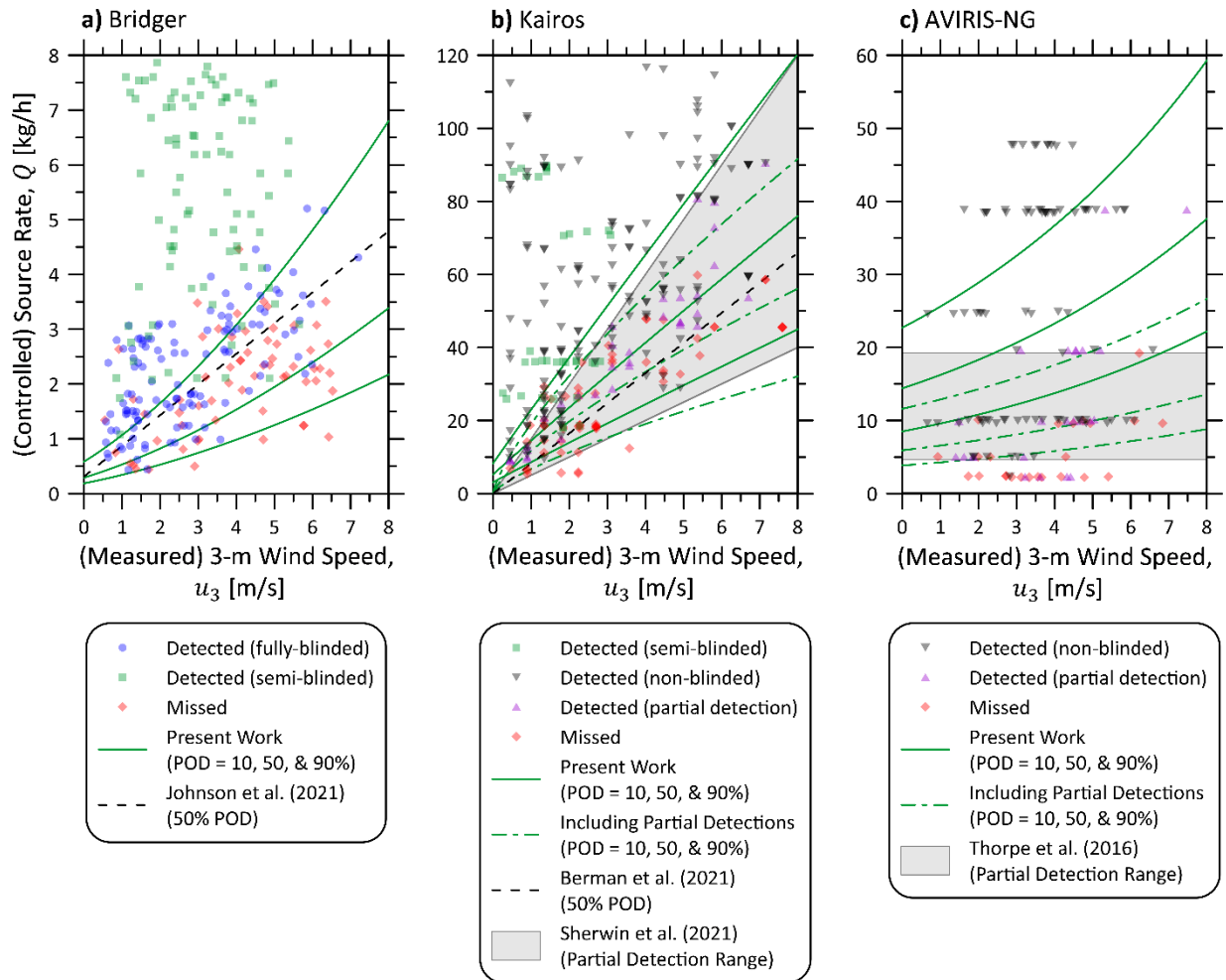
122

123

Figure S3: Histogram and fitted distribution for the 3-m wind speed relative error ratio (RER). (a)-(b) Bridger’s GML technology using MeteoBlue wind data as computed via Eq. (6) and (5) in the manuscript, respectively; The histogram in subplot (b) is shaded and the distribution is dashed to contrast it with the other plots, since the use of Eq. (5) in this case specifically considers day-to-day and site-to-site variability when determining the overall bias and precision; (c)-(f) Kairos’ LeakSurveyor Technology using four different sources of wind speed data computed via Eq. (6).

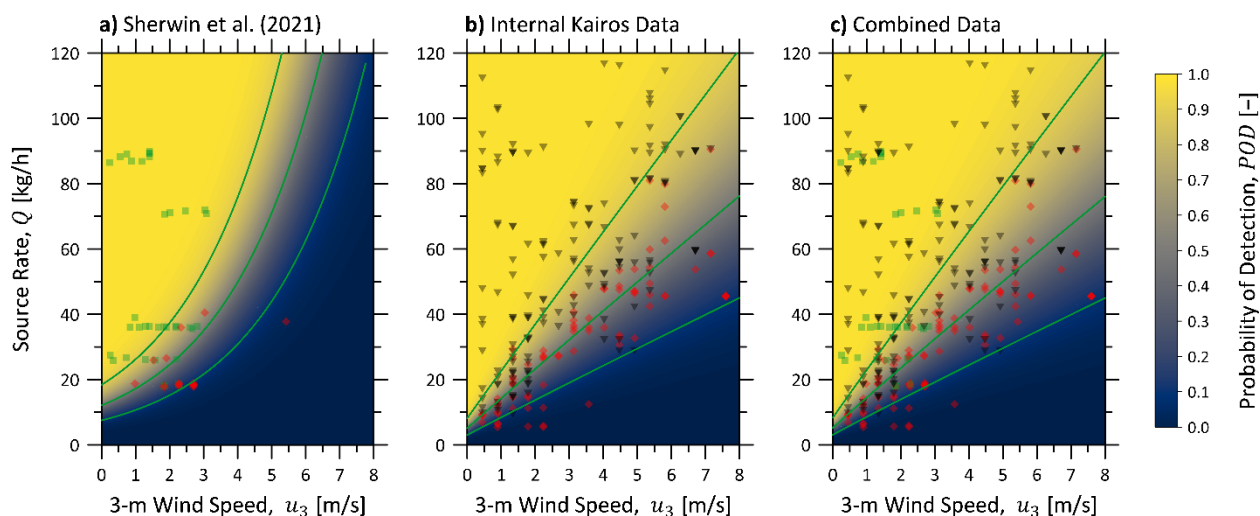
124 **S3 Additional Detail of Data used in POD Derivations**

125 The following figures support the discussion in the manuscript. Figure S4 plots available
 126 controlled release data for each measurement technology across all aircraft altitudes, the POD
 127 contours from the derived POD functions (replicated from the manuscript), and previously
 128 published detection sensitivities. Note that for each plot there are additional large-scale release
 129 data beyond the limits of the y-axis.



130
 131 **Figure S4: Comparison of probabilities of detections for Bridger's GML (a), Kairos' LeakSurveyor (b), and**
 132 **NASA JPL's AVIRIS-NG (c) technologies. Each figure plots probability contours using the present**
 133 **methodology (at 10, 50, and 90% POD) alongside available controlled release data, which included**
 134 **measurements across all flight altitudes and are coloured according to detection (black = unblinded, blue =**
 135 **fully blinded, green = semi-blinded) and miss (red). Each figure also identifies previously published estimates**
 136 **of detection sensitivity: 50% POD for Bridger's GML (Johnson et al., 2021) and Kairos' LeakSurveyor**
 137 **(Berman et al., 2021), and partial detection ranges for Kairos' LeakSurveyor (Sherwin et al., 2021) and NASA**
 138 **JPL's AVIRIS-NG (Thorpe et al., 2016).**

139 Figure S5 provides the optimized POD function using the methodology in the present work and
 140 controlled release data for Kairos' LeakSurveyor. Subplots a) through c) show significant
 141 differences in the optimized POD when using Sherwin et al.'s (2021) data alone (a; semi- and non-
 142 blinded detections and treating "partial" detections as misses), Kairos' internal controlled release
 143 data alone (b; non-blinded detections and treating "partial" detections as misses), and the
 144 combination of these data sources (c). These results identify that POD functions derived in the
 145 manuscript are dominated by Kairos' non-blinded internal data, which is unsurprising given that
 146 Sherwin et al.'s (2021) experiments yielded limited data near the detection limit as shown in Figure
 147 S5a. The different POD function when using Sherwin et al.'s (2021) semi-blinded data (Figure
 148 S5a), as compared to Kairos' non-blinded data (Figure S5b), also identifies the importance of
 149 rigorous experimental blinding and the need for further third-party experiments of Kairos'
 150 LeakSurveyor and AVIRIS-NG.



151
 152 **Figure S5: Optimized POD functions for Kairos' LeakSurveyor technology, ignoring partial detections using**
 153 **different data sets: a) the data of Sherwin et al. (2021) alone, b) the confidential data from Kairos' internal**
 154 **studies alone, and c) the combination of these data sources.**

155 S4 References

156 Akaike, H., 1974. A new look at the statistical model identification. *IEEE Trans Automat Contr* 19, 716–
 157 723. <https://doi.org/10.1109/TAC.1974.1100705>

158 Berman, E., S.F., W., B., E., Jones, B.B., 2021. Kairos Aerospace Technical White Paper: Methane
 159 Detection (Version 1F). Kairos Aerospace. <https://doi.org/10.17605/OSF.IO/HZG52>

- 160 Johnson, M.R., Tyner, D.R., Szekeres, A.J., 2021. Blinded evaluation of airborne methane source detection
161 using Bridger Photonics LiDAR. *Remote Sens Environ* 259, 112418.
162 <https://doi.org/10.1016/j.rse.2021.112418>
- 163 Kass, R.E., Raftery, A.E., 1995. Bayes Factors. *J Am Stat Assoc* 90, 773–795.
- 164 Sherwin, E.D., Chen, Y., Ravikumar, A.P., Brandt, A.R., 2021. Single-blind test of airplane-based
165 hyperspectral methane detection via controlled releases. *Elementa: Science of the Anthropocene* 9.
166 <https://doi.org/10.1525/elementa.2021.00063>
- 167 Snipes, M., Taylor, D.C., 2014. Model selection and Akaike Information Criteria: An example from wine
168 ratings and prices. *Wine Economics and Policy* 3, 3–9. <https://doi.org/10.1016/j.wep.2014.03.001>
- 169 Thorpe, A.K., Frankenberg, C., Aubrey, A.D., Roberts, D.A., Nottrott, A.A., Rahn, T.A., Sauer, J.A.,
170 Dubey, M.K., Costigan, K.R., Arata, C., Steffke, A.M., Hills, S., Haselwimmer, C., Charlesworth, D.,
171 Funk, C.C., Green, R.O., Lundeen, S.R., Boardman, J.W., Eastwood, M.L., Sarture, C.M., Nolte, S.H.,
172 Mccubbin, I.B., Thompson, D.R., McFadden, J.P., 2016. Mapping methane concentrations from a
173 controlled release experiment using the next generation airborne visible/infrared imaging
174 spectrometer (AVIRIS-NG). *Remote Sens Environ* 179, 104–115.
175 <https://doi.org/10.1016/j.rse.2016.03.032>
- 176